Imperial College London

MSC in Advanced Aeronautical Engineering

Imperial College London

Department of Aeronautics

Project Saturn

Studying the Aerodynamic Behaviour of a Circular Wing by Having a Radial Duct Blowing Air on It

By: **Saif Shraideh**

CID: **01426677**

Supervisor: **Dr. Aaron Knoll, PhD**

20th.September.2018

Abstract

In this day and age, the high demand for new tools to enhance aviation and urban transportation is higher than ever before. New concepts and design ideas are being tested to find new, safe, energy efficient, environmentally friendly ways of air transportation. This project aims to investigate a novel design for a flying vehicle which is comprised of a stationary circular wing with a radial duct forcing airflow over its surface. This paper focused on various critical factors concerning the design of this concept. A preliminary design was done to start the design process. Calculations were then carried out to estimate the design of the circular wing, duct, and the fan. Afterwards, a detailed Computational Fluid Dynamics (CFD) analysis was done to study and validate the aerodynamic behaviour of the design configuration. Finally, an experiment was performed by manufacturing and testing the model to validate the design, and to compare the results with the theoretical calculations and the CFD analysis. This paper physically demonstrated that the circular wing was able to generate lift force; however, the amount generated was very low. The aerodynamic behaviour of a circular wing with a radial duct forcing air over its surface was not as efficient as conventional methods of creating lift force. Nevertheless, the project showed a lot of potential since the experiment was successful, and there is much room for design improvement.

<u>Keyword's</u>

- Circular Wing
- Radial Flow
- Lift Force
- Computational Fluid Dynamic
- Performance

Acknowledgment

After an exhaustive 4-month period of completing my dissertation, writing this message of appreciation is the cherry on top. It has been a long and intensive journey filled with learning and enhancing my abilities to bring ideas to life. This journey was filled with great people who pushed me forward to reach the success at this stage in life. I would like to thank each and every individual who was in this adventurous path with me and would like to reflect my appreciation to them.

Firstly, I would like to thank my family members for supporting me and my idea and pushing me forward to actually make this idea my dissertation topic. Without you, the idea would probably have remained a drawing collecting dust in one of my old drawers. I would like to thank one of my greatest supporters, my supervisor Dr. Aaron Knoll, for believing in me and in the idea, as bold as it sounded at first. Thank you for accepting to supervise my project and thank you for believing in me. Without you, the project would have never reached this level of engineering sophistication and would not have moved forward.

I would also like to thank Roland Hutchins, Franco Giammaria, Alan Smith, and the rest of the team and lab technicians for helping me to manufacture the project. Working with an amazing team like you taught me a lot about practical work and ways to tackle problems. The lab experience that I gained is incomparable to any lab-based projects I have done before. Thank you all for your help and for your interest in this project.

Table of Contents

1. Nomenclature 4
2. Introduction 5
3. Background 7
4. Theory and Methodology 9
   4.1 Inner Workings of the Design 9
   4.2 Initial Design Dimensions 10
5. Design and Sizing Estimation 11
   5.1 Initial Estimation of Reynolds Number 11
   5.2 Airfoil Selection 12
   5.3 Initial Values Refinement 13
   5.4 Duct Exit Velocity Calculations 14
   5.5 Final Wing Sizing and Positioning 15
   5.6 Final Values Refinement 16
6. Computational Fluid Dynamics (CFD) Analysis 18
   6.1 2D Inviscid Flow Around the Airfoil 18
   6.2 2D Viscous Flow Around the Airfoil 21
   6.3 3D Flow Around a Straight Wing 26
   6.4 3D Flow Around a Circular Wing 27
   6.5 3D Flow Around a Straight Wing with a Duct 30
   6.6 3D Flow Around a Circular Wing with a Duct 31
      6.6.1 Duct Design 31
7. Centrifugal Fan Design 36
   7.1 Centrifugal Fan Inlet 37
   7.2 Centrifugal Fan Outlet 37
8. Stators Design 39
9. Experiment 40
10. Conclusion 41
11. References 42
12. Appendices 43

1. Nomenclature

L	Lift Force
ρ	Air Density
V	Air Velocity
C_L	3D Lift Coefficient
C_l	2D Lift Coefficient
C_{LMAX}	Maximum 3D Lift Coefficient
C_{lMAX}	Maximum 2D Lift Coefficient
A	Wing Area
$\Lambda_{c/4}$	Sweep Angle at Quarter-Chord
Re	Reynolds Number
l	Characteristic Length
α	Angle of Attack
Å	Airflow Area
h	Duct Height
r	Radius
V_{LE}	Air Velocity at Leading-Edge
V_{MC}	Air Velocity at Mid-Chord
R_{LE}	Radius of Wing's Leading-Edge
R_{TE}	Radius of Wing's Trailing-Edge
C_f	Friction Coefficient
C_p	Pressure Coefficient
$\Delta\dot{m}$	Net Mass Flux
C_d	2D drag Coefficient
a	Lift Curve Slope of a Finite Wing
a_o	Lift Curve Slope of an Infinite Wing
$\alpha_{L=0}$	Zero Lift Angle of Attack
AR	Aspect Ratio
τ	Function of Fourier Coefficient (A_n)
δ	Induced Drag Factor
S	Wing Span
C	Wing Chord
r_1	Centrifugal Fan Inlet Radius
r_2	Centrifugal Fan Outlet Radius
b	Centrifugal Fan Blade Height
N	Rotational Speed
$\dot{m}$	Mass Flow Rate
$\dot{Q}$	Volumetric Flow Rate
ω	Angular Velocity
β_1	Centrifugal Fan Blade Inlet Angle
β_2	Centrifugal Fan Blade Outlet Angle
V_{r1}	Relative Flow Velocity at Inlet
V_{r2}	Relative Flow Velocity at Outlet
V_{f1}	Flow Velocity at Inlet
V_{f2}	Flow Velocity at Outlet
U_1	Centrifugal Fan Linear Velocity at Inlet
U_2	Centrifugal Fan Linear Velocity at Outlet
V_1	Absolute Velocity at Inlet
V_2	Absolute Velocity at Outlet
α_2	Absolute Velocity Flow Angle at Outlet
V_{w2}	Whirl Velocity at Outlet

2. Introduction

At the dawn of aviation, the creation of flying crafts seemed impossible and was thought of as wizardry. The natural curiosity and persistence of mankind is what flared the creative mind to look around and imitate nature at its best. The simple idea of building a bird-like creation is what lead us to today's advancement: companies around the world competing over who made the fastest, most efficient, and safest aircraft. Over the years, the shape and design of the aircraft started to plateau, stabilizing into the familiar design of the commercial aircraft. While this design made the most sense, too much focus into improving this conventional design may cause us to miss out on other possibilities of flight designs that may prove to be better. This project aims to test a novel aircraft design, which is a continuation of a previous research paper done at the University of Exeter [1]. This design consists of a circular wing with an electric motor blowing air radially on it to provide vertical lift. The previous model can be seen in Figure (1) and (2), and the updated model can be seen in Figure (3).

The design discussed in this paper seeks to improve urban aviation in particular. This design could be used to transport people or goods from one place to another. Although the project concept uses similar aircraft technologies, it applies them in a different configuration that makes it novel. This could be advantageous in many different ways, such as potentially being safer, more stable, environmentally friendly, and more robust.

The main idea behind this project is to reverse engineer the concept of wings. In a conventional design, the wings are usually thrusted through the air to generate lift. Even in helicopters, the blades are spun slicing through air to create lift. However, doing the opposite, which consists of thrusting air along wings, may yield the same result, and therefore, could allow new wing designs. This phenomenon can be seen when testing scaled down aircraft models in a wind tunnel. In a wind tunnel, the model is rigged to the ground and connected to scales and computers. As the wind tunnel provides faster air flow, various forces, including the lift force, start to occur and increase. In this project, instead of using a wind tunnel, airflow is created using a centrifugal fan to thrust air along a circular wing.

This project is broken down into several sections, which will focus on the critical factors of the vehicle design, primarily the circular wing and its performance. An initial 2D design sizing was drawn based on the previous paper's design [1], and some minor calculations to adjust the previous design (Appendix A). A rough weight estimation was made to provide a starting point for the rest of the calculations, as the goal is to study the aerodynamics behaviour of a fully enclosed circular wing. Afterwards, wing analysis, consisting of wing sizing and refinement, in addition to wing positioning, was performed, followed by CFD simulations to cover the bases and to understand the general behaviour of the wing. The radial duct and centrifugal fan were designed to provide clean radial airflow towards the wing. Afterwards, the final vehicle design measurements were produced considering all the previous calculations and design optimizations (Appendix B). Finally, a 3D printed model was tested for aerodynamic behaviour and was compared to the CFD simulations and analytical solutions.

The aim of this project is to investigate a novel flying vehicle that is comprised of a stationary circular wing and forced air flow over its surface to understand its aerodynamic behaviour. This paper will discuss a scaled down version of the actual size which has a diameter of 4m [1]. The craft is scaled down 16 times to have a diameter of 0.25m. The objective of both the previous and current research, is to find a safer, more reliable, cost and energy efficient ways of aviation.

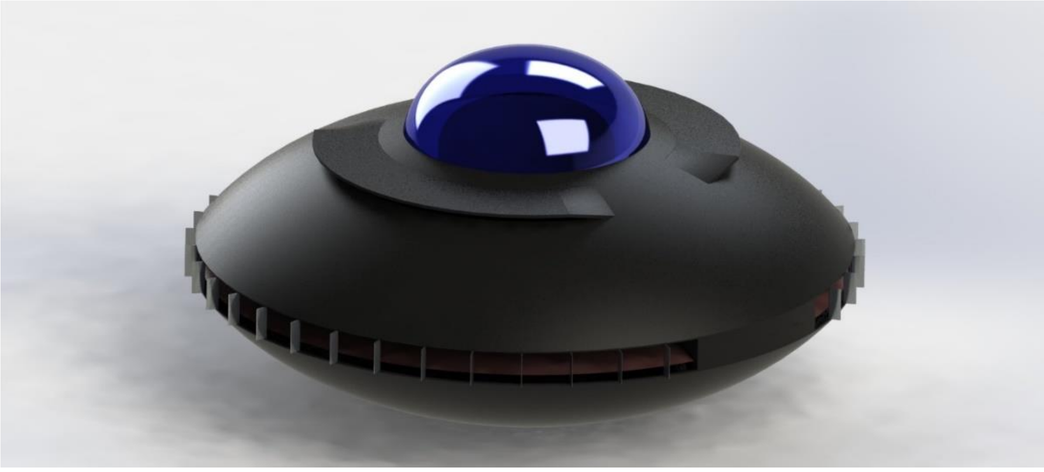

Figure (1): Isometric View of the Previous Model [1]

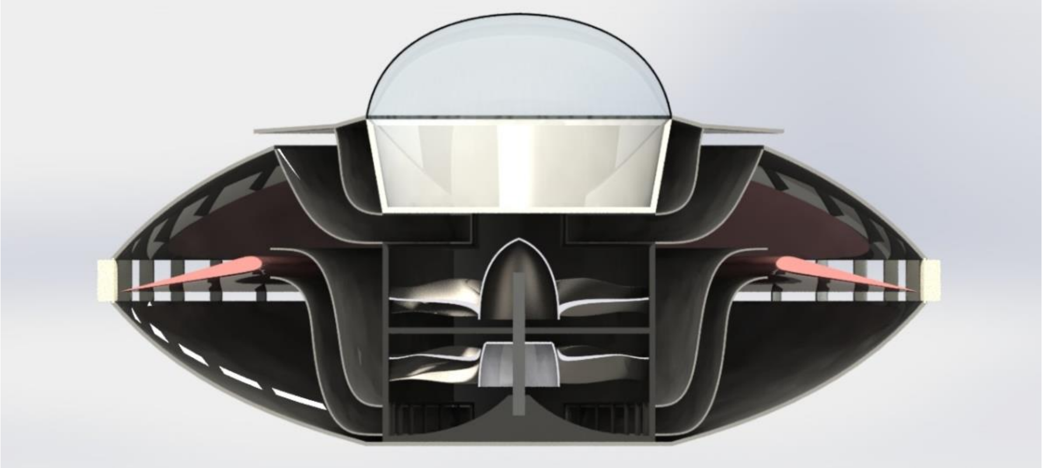

Figure (2): Cross-Section View of the Previous Model [1]

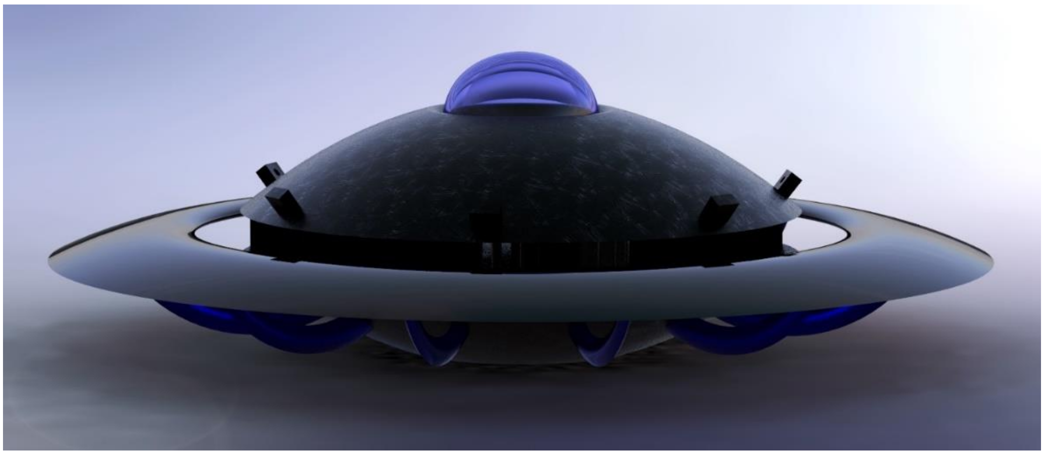

Figure (3): Isometric View of the Updated Model

3. Background

In the 1950s, the US Air Force worked on a classified project to build a supersonic flying saucer, with the code name 'Project 1794' [2]. The vehicle was developed by USAF and Avro Canada. The concept of the project was to create a self-propelling supersonic device that achieves 3 to 4 Mach [2]. The propulsion utilized the 'Coanda Effect' (the tendency of airflow to stick to a surface) to produce lift by having an outer disk-like component spinning at high speeds. Manoeuvrability was achieved by using small shutters placed at the edge of the disc [2] as shown in Figure (4). The power was provided by jet-turbines, and the design would allow the vehicle to perform vertical take-off and landing (VTOL) [2]. Project 1794 was concluded by a declassified memo, which stated that the vehicle could have a service ceiling of 100000 feet and a range of around 1850km (1000 nautical miles). However, there are no reports that state weather Project 1794 made it off the ground [2].

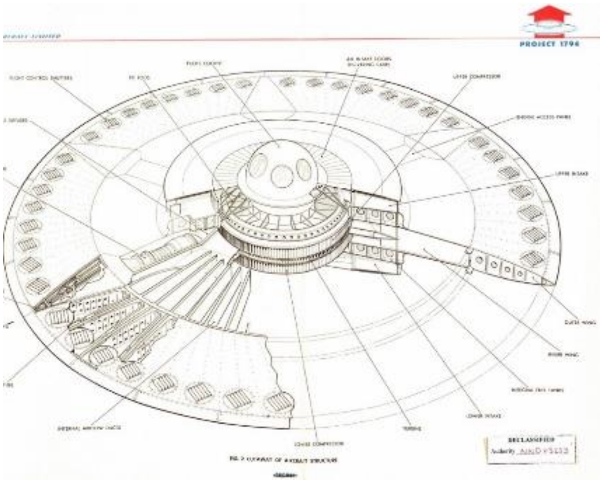

Figure (4): Project 1794 Cutaway Diagram [2]

In the same decade, Avro Canada worked on a similar project called 'VZ-9 Avro-Car' based on Project 1794, but smaller. It was capable of performing VTOL using the Coanda Effect and a single turbine fan to provide power by blowing air outside the circular edge of the vehicle, as shown in Figures (5) and (6) [3]. The project was intended to move at a speed of about 185km/hr (100kt), with a service ceiling of about 10000ft [2], [4]. Nevertheless, the Avro-Car showed unsolved thrust and stability issues [3]. It was difficult to control the vehicle due to its sensitive controls, and any weight instability could greatly impact the crafts stability. It was designed to carry two pilots on opposite sides in separate cockpits, further adding to its instability. The vehicle could not fly more than 3ft high due to instability [4]. Eventually, the project was cancelled in 1961 due to lack of funding.

Figure (5): Side View of Avro-Car [3]

Figure (6): Top View of Avro-Car [3]

In 2017, a project was done at the University of Exeter that covers similar basis of technology of Project 1794 and Avro-Car. The concept of that project was to design an electric vehicle which is stable, safe, environmentally friendly, and efficient, and could be used for urban transportation. As shown in Figures (1) and (2), the vehicle used a set of jet-turbines powered by a 'Siemens' electric motor to provide airflow to two semi-circular stationary wings to provide lift. The vehicle could perform VTOL, and manoeuvrability was achieved by using a set of air-blades located at the outer edge of the circular vehicle as shown in Figure (1), in which they can rotate on their axis. On paper, the project proved successful in many different aspects: it was able to provide enough lift to lift the 1tonn vehicle off the ground. Stability was achieved due to the circular wing design, which provided a lift force the goes around the vehicle from the outside. By analogy, if a person carrying a tray filled with cups of water holds it at the edges, it gives them complete control over the tray's stability. The vehicle adopted the same concept [1].

In terms of safety, the vehicle was made of fibre-impregnated polymers like carbon fibre, giving the best strength to weight ratio. Additionally, the design adopted a technology extensively used in Formula 1 racing, known as crash zones. In Formula 1 racing, the vehicles tend to have several aerodynamic shelled components that serve as crash safety measures. The nose cone of the vehicle is a great example: it provides the majority of the down force, but in the case of head on impact, the nose cone crumbles extending the time of impact and absorbing most of the impact force. The flying vehicle adopted the same concept as all the components serve dual functionality, both to move the air to the stationary wing, and to absorb impact forces in the case of an impact. Moreover, the advantage of such a design is that it is small enough that it can be fitted with a parachute, not only saving the pilot, but also the vehicle [1].

The vehicle was designed to be environmentally friendly in terms of noise levels and carbon footprint. It was meant to produce minimum noise levels as it would be used in urban areas. The ducted fan technology with minimum fan duct clearance increased the fan's efficiency. This produced more airflow at a lower engine power intake, thus reducing the noise when lifting off. In addition, the duct itself reduces the aerodynamic noise that is produced from the blade tips of the fans. Furthermore, the carbon footprint of the vehicle is zero. Power is provided electrically by a Siemens electric motor, which is powered by Lithium Polymer Batteries and a set of single crystalline solar cells. The single crystalline solar cells provided the highest efficiency of all other types of solar cells, which compensated for the weight penalty it implied. The batteries would be charged using a charging station on the ground and the solar cells [1].

Generally, the project showed great promise and was theoretically plausible. The use of two stationary semi-circular wings as the primary mean to provide the vertical lift force was the novel concept when compared to other aviation projects. Normally, all vehicle that perform VTOL use fans, propellers, or some form of a thruster to produce the necessary lift force. However, it still remained a mystery if the circular wing design could practically provide the necessary performance to lift the object off the ground.

4. Theory and Methodology

4.1 Inner Workings of the Design

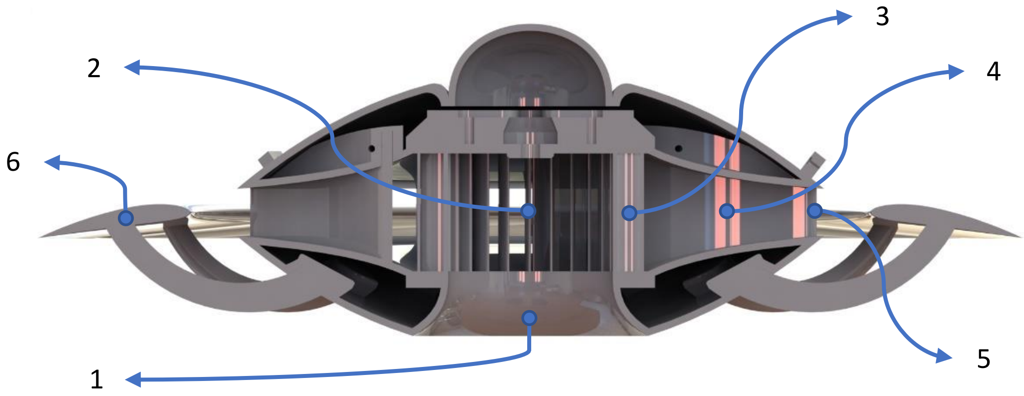

Figure (7): Cross-Section of Rendered Final Design

The concept of the vehicle design was to transport a sufficient amount of airflow towards the stationary circular wing, so that a sufficient amount of lift force was created to lift the vehicle off the ground. It involves six stages to guide the airflow cleanly and efficiently to the wing. The design functions of the scale model follow these stages, as seen below.

Stage 1: The air close to the inlet underwent a reduction in pressure and was therefore guided into and through the inlet passage. The inlet has a rounded contour that reduced in diameter as it nears the centrifugal fan. This caused the airflow to speed up, further reducing its pressure and sucking more air towards the inlet.

Stage 2: The air reached the centrifugal fan and experienced a rotation of 90^{o} towards the horizontal. The kinetic energy of the air increased and acted as the main driver to push airflow towards the duct.

Stage 3: The excited airflow moved towards the inlet of the duct, where it encountered stators. The stators gradually changed in direction, to correct the flow direction due to swirling velocity components such that the flow become purely radial.

Stage 4: The air flowed through the duct in a radial manner. The duct design converged to maintain flow velocity before it reached the duct exit.

Stage 5: The airflow moved at a specified velocity in a pure radial direction as it exited the duct. The duct was designed to maintain atmospheric air pressure so that when the air left the duct, it moved toward the circular wind in a clean radial stream of air.

Stage 6: The airflow reached the circular wing, which was mounted by 12 connection arms at a designed angle of attack, and therefore, lift was generated.

4.2 Initial Design Dimensions

The general dimensions of some critical features of the preliminary scale model served as a starting point for the design calculations. The following image shows the preliminary design of the scale model.

Figure (8): Cross-Section of Rendered Preliminary Design

The preliminary dimensions are shown below.

- Overall diameter: **0.4m**
- Wing's leading-edge radius: **0.15m**
- Wing's trailing-edge radius: **0.2m**
- Wing chord: **0.05m**
- Duct exit radius: **0.125m**
- Duct height: **0.01m**
- Impeller radius: **0.1m**

5. Design and Sizing Estimation

In the previous research upon which this paper is based [1], the vehicle was designed such that its actual size was a diameter of 4m, resembling that of a large family car. However, the vehicle was scaled down by 16 times, resulting in a diameter of 0.25m, to produce a more manageable design for testing, and cheaper for manufacturing.

This paper's vehicle was designed using SolidWorks to estimate the relative size of the components to each other and to have an initial mass estimation. The preliminary design of the vehicle is shown in Figures (9) and (10) below. The sizing of the current model was based on the previous research [1], in addition to education intuition and trial and error regarding the size of separate elements relative to each other. The exact dimensions of the initial sizing are in Appendix (A). The mass of the vehicle was not an important parameter at this stage, and only served as a design starting point from which the calculations could start.

Figure (9): Isometric View of the Scale Model

Figure (10): Cross-Section of the Scale Model

After assembling all the components together in SolidWorks, using a measurement tool provided by the program, the total volume of the vehicle was $940514.90\times10^{-9}m^3$. The measurements were obtained in millimetres and converted into meters to increase the accuracy. The vehicle was designed to be manufactured from Acrylonitrile Butadiene Styrene (ABS) plastic, which has a density of about $1052kgm^{-3}$ [5] as obtained from the SolidWorks database. The mass was then calculated to be 0.9894kg, which was rounded up to 1 kg.

The mass of the electric brushless motor could be estimated and is in the range between 20g-250g as the scaled model is in the size range of RC aircrafts and drones [6]. For the initial estimation, the brushless motor was assumed to have a mass of 300g. The mass was assumed higher in the calculations as a provisional measure to compensate if a larger motor is required. However, as the power supply would be mounted outside the vehicle from an external device, there was no battery dead weight included in the mass calculations. As aforementioned, the mass calculations served only as a design starting point. The calculations including all the components of the vehicle provide a total mass of 1.3kg. Therefore, the circular wing must produce a minimum lift force of 12.753N.

5.1 Initial Estimation of Reynolds Number

An initial estimation of the Reynolds number (Re) was required for a comparison analysis to select the most appropriate airfoil. The following lift equation was used to estimate the velocity:

$$\mathrm{L} = \frac{1}{2}\rho \mathrm{V}^2 \mathrm{C_L} \mathrm{A} \qquad \text{Eq. (1)}$$

$\mathrm{C_L}$, the 3D lift coefficient was crudely estimated by the following equation created for subsonic aircrafts with moderate wing sweep, [7]:

$$\mathrm{C_{L_{max}}} = 0.9\mathrm{C_{l_{max}}} \cos\Lambda_{c/4} \qquad \text{Eq. (2)}$$

Although Eq. (2) applies for a max 2D lift coefficient, the 2D C_l value used was high enough which allowed the use of Eq. (2). Since the circular wing has no sweep angle, Eq. (2) was reduced to:

$$C_{L_{max}} = 0.9C_{l_{max}} \qquad \text{Eq. (3)}$$

After obtaining the velocity, the Reynolds equation was used to estimate the Reynolds number:

$$Re = \frac{\rho V l}{\mu} \qquad \text{Eq. (4)}$$

The minimum lift force required was found to be 12.753N, with air density taken as 1.225kgm^{-3} at sea level. The circular wing had a leading-edge (LE) radius of 0.15m and a trailing-edge (TE) radius of 0.2m, so the wing area was: $\pi(0.2)^2$-$\pi(0.15)^2$ = $\underline{54977.87\times10^{-6}m^2}$. Lastly, an initial estimation of C_l was made and it equalled to 1. By using Eq. (1) and (2), the velocity is as follows:

$$C_{L_{max}} = 0.9\times1$$

$$12.753 = \frac{1}{2} \times 1.225 \times V^2 \times 0.9 \times 54977.87\times10^{-6} \longrightarrow \underline{V = 20.51ms^{-1}}$$

The dynamic viscosity of air at 15°C is μ = 1.7965×10^{-5}kgm^{-1}s^{-1} [8]. Therefore, the Reynolds number is:

$$Re = \frac{1.225\times20.51\times0.05}{1.7965\times10^{-5}} \longrightarrow \underline{Re = 69931.58 \approx 70000}$$

5.2 Airfoil Selection

Based on the Reynolds number obtained, 25 airfoils of various characteristics [9], which are listed in Table (1) below, were tested using 'xflr5' (uses 2D panel method). The airfoil with the highest lift to drag ratio was chosen for the scale model. Refer to Appendix (C) for airfoil geometries and shapes:

Table (1): List of test-airfoils

NACA Series Airfoils	Helicopter Rotor Airfoils	High Lift Airfoils	Low Reynolds Airfoils	High Lift Low Reynolds Airfoils	Wind Turbine (High L/D) Airfoils
(naca4412)	(ah79100c-il)	(la203a-il)	(dae11-il)	(ch10sm-il)	(ah93w145-il)
-	(hh02-il)	(e423-il)	(dae31-il)	(e387-il)	(sg6040-il)
-	-	(fx74modsm-il)	(e205-il)	(fx63137-il)	(sg6041-il)
-	-	-	(e66-il)	(fx63137sm-il)	(sg6042-il)
-	-	-	(rg15-il)	(miley-il)	(sg6043-il)
-	-	-	(s2027-il)	(s1223-il)	-
-	-	-	(s7055-il)	-	-
-	-	-	(s8036-il)	-	-

<u>'xflr5' tests analysis parameters are the same for all the airfoils and all further analysis:</u>

- Reynolds Number: **70000**
- Number of Panels: **300**
- TE/LE Panel Density Ratio: **1**
- Range of Angles of Attack: **0:0.5:15**
- Number of Maximum Iterations: **100**
- Forced Transition:
    - Top Transition Location (x/c) = **1**
    - Bottom Transitions Location (x/c) = **1**

The analysis results from xflr5 are shown in Figure (11) below, the rest of the graphs including the lift and drag coefficients are in Appendix (D). There were extensive variations between the curves and high irregularities within each curve. The presence of such anomalies was due to a very low Reynolds number, which introduced the presence of a laminar separation bubble and full or partial flow detachment for some airfoils at certain angles of attack. As aforementioned, the analysis was done to find the airfoil with the highest L/D, and it is the 'SG6043' airfoil, its curve is coloured in bright red.

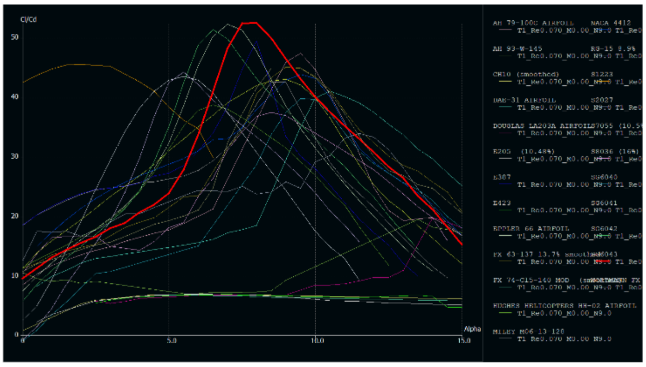

Figure (11): L/D Graphs for 25 Airfoils at Re=70000

The airfoil 'SG6043' gave the best performance having a L/D = 49.85, C_l = 1.458 at α = 8°. However, it was not chosen for few reasons. First, due to its complex geometry: when performing the CFD analysis, ANSYS Mesher was not able to mesh the geometry without showing errors. Additionally, the TE of the airfoil is very sharp and steep, which will create problems when 3D printing the wing, due to the lateral process that the printer undergoes when adding the layers. It would cause the wing to be either very fragile to handle, and/or the layers at the TE will collapse and destroy the whole wing. Therefore, the analysis was continued with a different airfoil: 'NACA 4412'. The airfoil's geometry is far simpler than 'SG6043', which compensated for the performance loss as seen in the comparison in Figure (12). The 'NACA 4412' provided L/D = 43.74, C_l = 1.365 at α = 9.5° at the same Reynolds number of 70000.

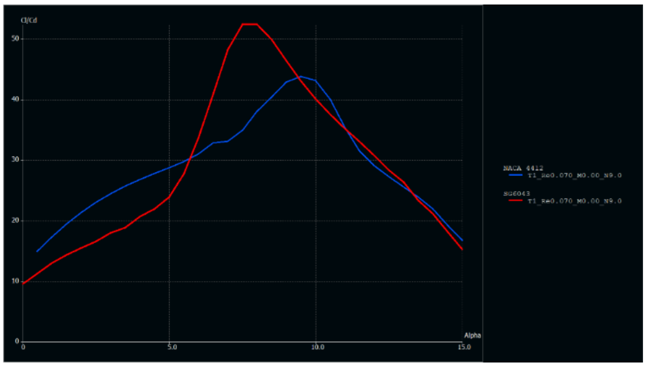

Figure (12): L/D Comparison Between 'SG6043' and 'NACA 4412' at Re=70000

5.3 Initial Values Refinement

An iterative process took place to find the exact lift coefficient and air velocity values. Eq. (1) and Eq. (3) were used to calculate the velocity, which was then used in Eq. (4) to find Reynolds number. Finally, the Reynolds number was used in xflr5 to reanalyse the chosen airfoil and to find the 2D lift coefficient. The same process was repeated until the values converged and stabilized. The process started with the 'NACA 4412' values as initial conditions as shown below:

- Lift (L) = **12.753N**
- Density (ρ) = **1.225kgm^{-3}**
- C_l = **1.365 @ α = 9.5°**

Since the wing is circular, any change in the angle of attack changes the radius of LE and/or TE, and this changes the wing area. Subsequently, the angle of attack increased from 9.5° to 10°, this reduced the wing area from $54977.87 \times 10^{-6} m^2$ to $54870.16 \times 10^{-6} m^2$. The change in area was only 0.2% which is negligible, thus the new area will be set constant for further calculations. The velocity is V = $17.5751 ms^{-1}$, by using the velocity obtained:

Iteration [#1]: V = $17.5751 ms^{-1}$ ➔ Re = 59920.6218 ➔ $C_l = 1.368$ @ $\alpha = 10°$

Iteration [#2]: V = $17.5558 ms^{-1}$ ➔ Re = 59854.8833 ➔ $C_l = 1.368$ @ $\alpha = 10°$

Iteration [#3]: V = $17.5558 ms^{-1}$ ➔ Re = 59854.8833 ➔ $C_l = 1.386$ @ $\alpha = 10°$

So, the values stabilized, and the results are:

V = $17.5751 ms^{-1}$ ➔ Re = 60000 ➔ $C_l = 1.386$ @ $\alpha = 10°$

Airflow slows down as air moves radially outward, such that the velocity at the LE will be faster than that at the TE. The rate at which the velocity slows reduces as the radius increases as shown in Eq. (7) and Appendix (E). But for simplicity, the velocity will be assumed that it slows down at a constant reduction rate (linearly) only across the chord for only this step, this helped to assume that the velocity obtained above was the average velocity across the wing chord. Therefore, it can be thought of as the velocity of the vertical plane coinciding with the mid-chord of the wing as shown in the figure below. This assumption helped in the calculations in the following section.

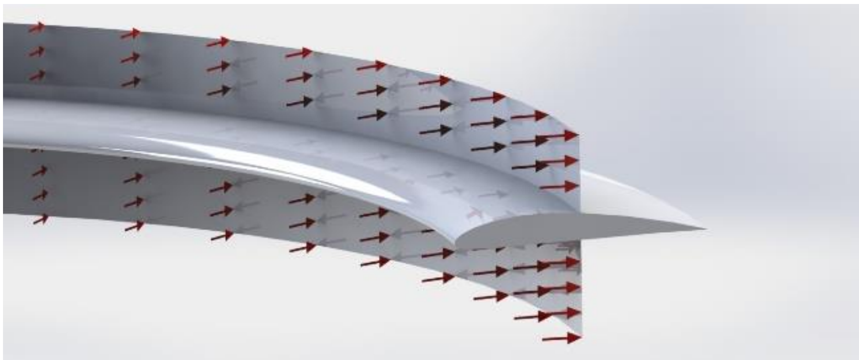

Figure (13): Predicted Velocity Profile of the Vertical Plane at the Mid-Chord

5.4 Duct Exit Velocity Calculations

The calculations within this section used the mass continuity equation as shown below to obtain the duct exit velocity required. This value assisted in obtaining the proper centrifugal fan design and the power required, such that the fan delivered the right air velocity to the circular wing:

$$\rho_1 \mathring{A}_1 V_1 = \rho_2 \mathring{A}_2 V_2 \quad \text{Eq. (5)}$$

Some assumptions were made to assist calculations. First, air is incompressible. Second, the air exiting the duct has the same pressure as the ambient pressure (101325Pa). The pressure assumption helped to idealize the airflow, such that the airflow could be thought of moving straight out of the duct with a constant height without being over or under expanded, as shown in Figure (14). If the pressure at the exit was not equal to the ambient pressure, this could create undesirable vortices and/or flow reversal. The flow was assumed to move straight (constant height 'h') to simplify calculations as seen in Figure (14). The assumptions served the purpose of the initial design estimation.

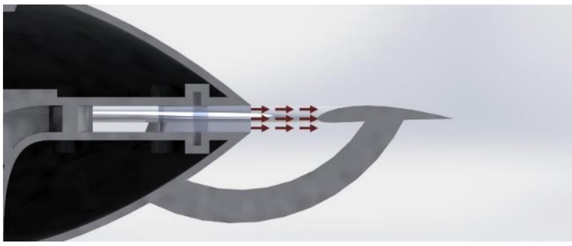

Figure (14): Cross-Section View of the Exit Duct and Air Flow Path to the Wing

The flow area was calculated as:

$$Å = 2\pi rh \qquad \text{Eq. (6)}$$

Where ‘h’ and ‘ρ’ are constants, this will reduce Eq. (5) to:

$$r_1V_1 = r_2V_2 \qquad \text{Eq. (7)}$$

The mid-chord had a radius of 0.175m, with an average velocity of 17.5751ms^{-1}. The wing’s LE radius was 0.15m, by using Eq. (7) the velocity there was found to be 20.5043 ms^{-1}. Eq. (7) was used again to obtain the velocity at the exit of the duct. The radius at the duct exit was 0.125m, and so the duct exit velocity was 24.6051ms^{-1}. The same calculations can be obtained from the graph provided in Appendix (E).

5.5 Final Wing Sizing and Positioning

The wing was tested for lift force at every horizontal position at all the chord lengths possible, while setting the duct exit velocity to be constant at 24.6051ms^{-1}. This analysis helped to find the maximum lift that can be produced with the minimum velocity exiting the duct, while monitoring the weight change of the vehicle as the wing size changes. The goal was to find the maximum lift force with the least power input while monitoring the weight. The underlying theory was that by shifting the wing closer to the duct, the average velocity over the wing would increase causing an increase in the overall lift force. However, by shifting the wing inwards, both the LE and TE radii were reduced, and thus reduced the wing area and the lift force.

Subsequently, the TE radius was set constant and the LE radius was reduced by shifting the LE inwards closer to the duct. The lift force was increased by 2 factors; due to the increase in wing area, and an increase in the average velocity. However, this increased the overall weight of the vehicle, which reduced the effectiveness of the enhanced lift. As the weight was only estimated to have a design starting point, the increase in weight was not a significant problem. The outcome of this analysis was to have the wing with the largest possible wing area and as close as possible to the exit duct.

The analysis started using some previous values as initial conditions as shown below. Also, a constraint was added such the wing’s LE cannot be closer than 1cm to the exit duct, anything closer than that can result in pressure rise distorting the airflow around the wing.

Initial Conditions:

- Duct Exit Velocity: **24.6051ms^{-1}**
- Duct Exit Radius: **0.125m**
- Wing Leading-Edge Radius: **0.15m**
- Duct-Wing Leading-Edge Clearance: **0.025m**
- Wing Chord length: **0.05m**
- Airfoil: **‘NACA 4412’**

For the analysis, the wing started at its initial position as stated in the 'Initial Conditions list above'. The chord then was elongated by increments of 1mm up to 0.065m (1cm clearance) with the TE radius constant. The process was then repeated with the initial conditions, but the whole wing was shifted by 1mm inwards. The TE radius was set again as constant, and the chord length was elongated by increments of 1mm until reaching a chord length of 0.064m.

The process was repeated until all the available positions with varying wing chords were included. The final step concluded at the LE having a radius of 0.135m and a chord length of 0.065m. The data is available in Appendix (F). At each increment, the average velocity was calculated by the following equation:

$$V_{MC} = \frac{R_{LE} \times V_{LE}}{\left(\frac{R_{TE}-R_{LE}}{2}\right)+R_{LE}} \qquad \text{Eq. (8)}$$

Where 'V_{LE}' is the wing's LE velocity:

$$V_{LE} = 3.0756(R_{LE})^{-1} \qquad \text{Eq. (9)}$$

Eq. (8) and (9) were customized equations for this vehicle's design. Both equations are based on the mass continuity equation and strictly on having an exit duct radius of 0.125m and an exit duct velocity of 24.6051ms^{-1}. By specifying a LE radius, Eq. (9) produced the velocity at that radius specified. The theory behind Eq. (9) can be found in Appendix (E). However, Eq. (8) specifies the average velocity (velocity at mid-chord) for any wing size at any position required, by only specifying the LE and the TE radii. Eq. (9) have the same restrictions as Eq. (8).

After finding the velocity, Reynolds number was calculated using Eq. (4) and then used in xflr5. Afterwards, Eq. (3) was used to approximate the 3D lift Coefficient 'C_L'. Finally, Eq. (1) was used to find the lift force produced by the wing.

The wing sizing and positioning was chosen to obtain the maximum lift force, and therefore the weight increase was irrelevant. The wing chord was increased from 0.05m to 0.065m, the wing's LE radius was reduced from 0.15m to 0.135m. The TE radius remained at 0.2m. The wing area increased from 54870.16×10^{-6}m^2 to 68408.18×10^{-6}m^2. The wing now had a 2D lift coefficient of 1.353 at α = 9° and produced a lift force of 17.202N, about a 26% increase in lift force due to optimizing the wing and maintaining the duct exit velocity at 24.6051ms^{-1}.

5.6 Final Values Refinement

While the wing sizing and positioning was all set, the new lift force obtained was 26% greater than the initial lift force estimation of 12.753N. By reducing the lift required from 17.202N to 12.753N, this will comply with the initial lift force estimation but with reduced duct exit velocity. This means that less power will be required to produce the same amount of lift. By using Eq. (1) and (3) and the new conditions stated below, a new average velocity will be calculated as follows:

New Conditions:

- Lift (L) = **12.753N**
- Density (ρ) = **1.225kgm^{-3}**
- C_l = **1.353 @ α = 9°**
- Wing Area (A) = **68408.18×10^{-6}m^2**

The average velocity (velocity at mid-chord) was found to be 15.8099ms^{-1}. Another iterative process took place to refine the average velocity by using Eq. (4) to find Reynolds number, then xflr5 for the

2D lift coefficient, followed by Eq. (1) and Eq. (3) to find the average velocity. This was repeated until the results converged:

Iteration [#1]: V = 15.8099ms^{-1} ➔ Re = 70073.0766 ➔ C_l = 1.364 @ α = 9.5°

Iteration [#2]: V = 15.7460ms^{-1} ➔ Re = 69789.9619 ➔ C_l = 1.365 @ α = 9.5°

Iteration [#3]: V = 15.7402ms^{-1} ➔ Re = 69764.3832 ➔ C_l = 1.365 @ α = 9.5°

Iteration [#4]: V = 15.7402ms^{-1} ➔ Re = 69764.3832 ➔ C_l = 1.365 @ α = 9.5°

After the values stabilized, and the final results were:

V = 15.7402ms^{-1} ➔ Re = 70000 ➔ C_l = 1.365 @ α = 9.5°

Finally, Eq. (7) was used to find the air velocity at the duct exit. This value dictated the design of the air duct and the centrifugal fan that was used to move air. The mid-chord radius for this optimised wing was 0.1675m, and the velocity there was 15.7402ms^{-1}. The LE radius was 0.135m, by using Eq. (7), this gave a LE velocity of 19.5295ms^{-1}. Using the same equation, the duct exit velocity was found to be 21.0919ms^{-1}. The duct exit velocity was reduced by approximately 14.3% from the initial estimation of 24.6051ms^{-1}.

Since the Reynolds number is very low (Re = 70000), there was a laminar separation bubble as shown in Graph (1). Reynolds number was reduced further because the air moving on top of the wing slowed down as it moved radially outward. This could cause undesirable flow separation. This is mainly why the wing's Reynolds number was obtained from the wing's mid-chord, or by averaging the velocity, it is more accurate. Calculating it from the LE lowered the Reynolds number even further, and therefore, may cause flow detachment. Two solutions were examined to correct this problem. The first was to add vortex generators right above the LE; however, adding vortex generators is not possible for this scaled model as they were small and ineffective. And the second was to increase flow velocity. The selected solution was to increase the flow velocity to increase Reynolds number.

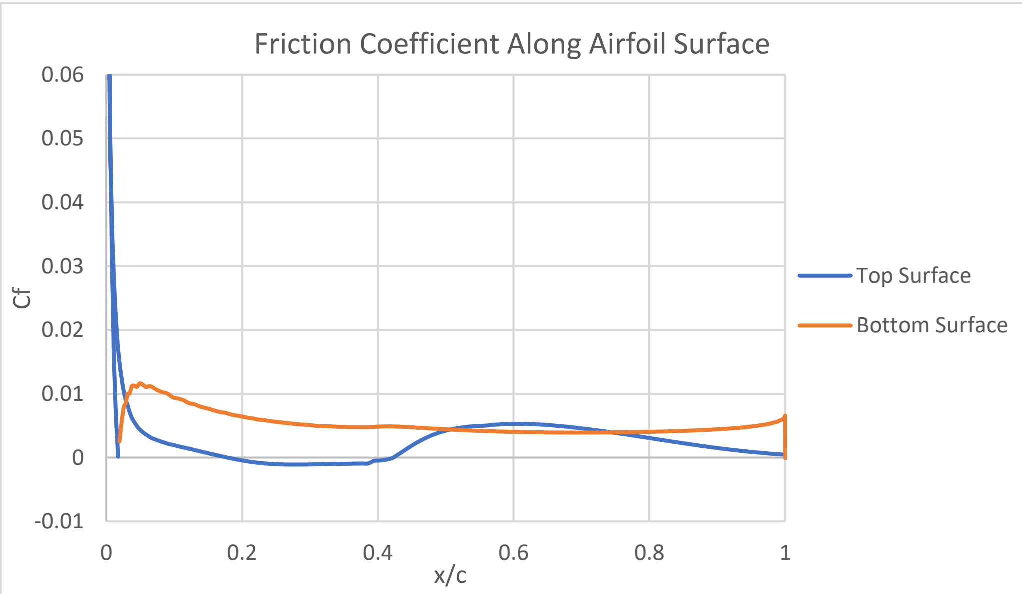

Graph (1): xfoil Friction Coefficient along the Airfoil Surface 'NACA 4412' at Re=70000

6. Computational Fluid Dynamics (CFD) Analysis

The following section serves to study the flow around the 3D circular wing and to understand the flow behaviour around it. It targets questions such as: will the value of lift force vary from a conventional wing shape? If yes, by how much it will differ? Will the circular wing provide sufficient lift? Based on the answers, final adjustments to the wing design were made before 3D printing the scale model. The CFD analysis was divided into 6 sub-analysis stages before reaching the final stage. The final and most important stage tested the circular wing with a duct in front of it. The 6 stages of analysis are:

1) <u>2D inviscid flow around the airfoil:</u> This analysis helped find the best mesh to be used for the later stages.

2) <u>2D viscous flow around the airfoil:</u> This analysis helped find the best turbulent model to be used for later stages.

3) <u>3D flow around a straight wing:</u> This stage served as a reference point for later stages to be compared with.

4) <u>3D flow around a circular wing:</u> This stage helped to understand the general behaviour of a circular wing facing a radial free stream of air.

5) <u>3D flow around a straight wing with a duct:</u> This stage helped to understand the effect of an air duct placed in front of a wing.

6) <u>3D flow around a circular wing with a duct:</u> This stage proved the validity of the concept.

6.1 2D Inviscid Flow Around the Airfoil

This section tested two types of meshes, one of which was used to calculate the flow around the airfoil and the wing in later stages. As aforementioned, the airfoil was changed from 'SG6043' to 'NACA 4412' due to meshing issues. The coordinates of 'NACA 4412' where obtained from xfoil where the coordinates are already coded; however, the issue was that the airfoil had an open TE. The simple geometry of 'NACA 4412' allowed slight modifications to close the TE using Excel. Afterwards, the airfoil was transferred to ANSYS Mesher to produce the two types of meshes: the structured C-Mesh and the unstructured high-resolution mesh as shown in Figures (15) and (16) respectively.

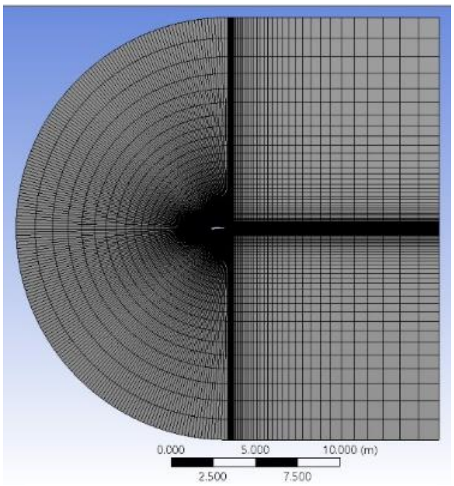

Figure (15): Structured C-Mesh

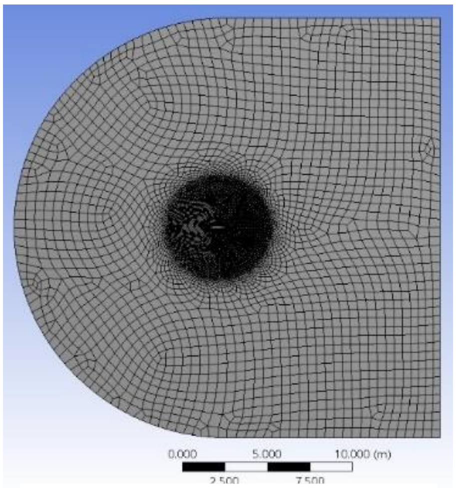

Figure (16): Unstructured Mesh

The meshes were made on the same airfoil and flow domain geometry. The airfoil had a chord length of 1m and the flow domain extended approximately 12.5m from the centre of the airfoil. The C-Mesh had 15000 cells and the unstructured mesh had 22894 cells. Both meshes were transferred to Fluent solver, and both tests had identical physical and numerical setups shown in Appendix (G). The airfoil was at an angle of attack (AoA) of 0^{o} to further simplify the analysis. After convergence, the pressure coefficient along the airfoil's surface was obtained and compared with results obtained from xfoil. The results are shown in Graphs (2) and (3), the blue dots are xfoil and the orange dots are ANSYS Fluent.

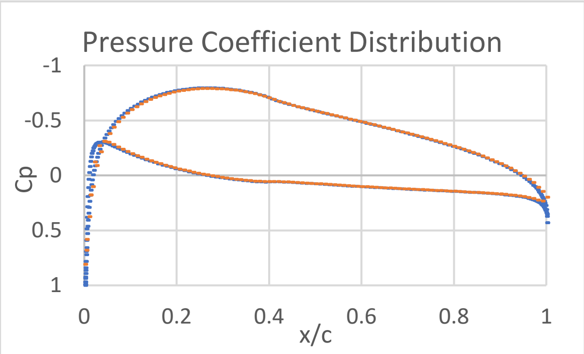

Graph (2): Pressure Coefficient Comparison Between xfoil and Structured C-Mesh

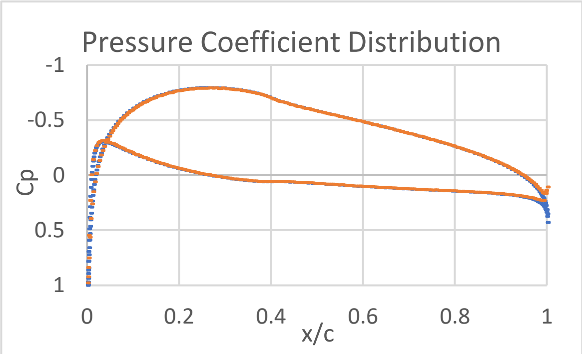

Graph (3): Pressure Coefficient Comparison Between xfoil and Unstrucured High-Resolution Mesh

As shown above, the pressure coefficient values were very similar to those obtained by xfoil. However, at the TE for both graphs, the pressure coefficient values tended to decrease a little bit. The linearization numerical errors were avoided by reducing the convergence absolute criteria to 1×10^{-6}. In other words, the solver kept on iterating until the pressure coefficient values stabilized, such that the change was negligible in the order of 10^{-4} to 10^{-5}. Therefore, the error could be due to not having a fine enough mesh, or due to TE modification.

What resulted in the error was found by refining both meshes, the C-mesh was refined to 40000 cells and the unstructured mesh to 67171 cells, this process also reduced the numerical discretization errors. Afterwards, the same physical and numerical setups as the previous test were applied, 'Appendix (G)'. The pressure coefficient graphs are shown below, where the blue dots are xfoil and the orange dots are ANSYS Fluent.

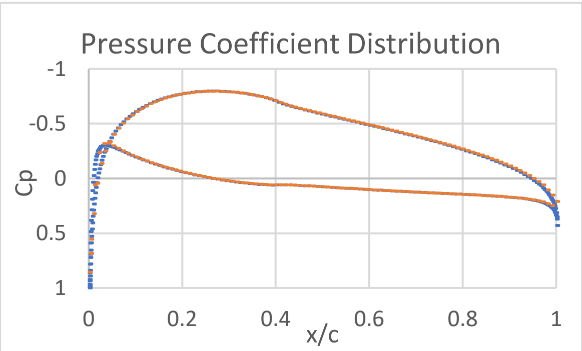

Graph (4): Pressure Coefficient Comparison Between xfoil and Structured C-Mesh Refined

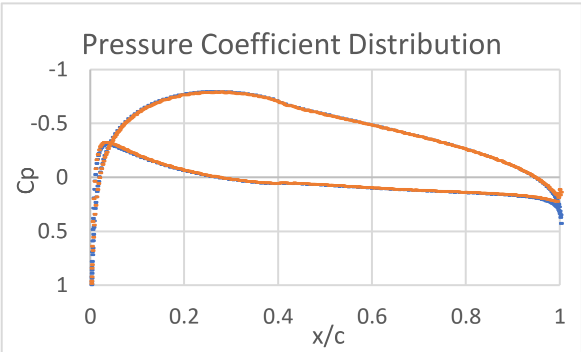

Graph (5): Pressure Coefficient Comparison Between xfoil and Unstrucured Mesh Refined

The new graphs showed very similar results; however, the pressure coefficient at the TE was still slightly pointing up. The mesh not being refined enough was eliminated as a reason due to low discretization errors. The values from Fluent solver could be trusted, because after performing the mesh refinement the results are approximately the same. The grid independence study (Mesh Refinement) had a tolerance of about 5%, mesh refinements stopped when the values of interest had 5% or less deviation from the previous mesh refinement results. This argument was backed up by looking at the net mass flux and coefficient values. In each cell, the net mass flux should ideally be zero, thus, the net mass flux over the flow domain should be zero. Also, the lift coefficient values should be similar to that of xfoil. The following results in Table (2) show the net mass flux between the inlet and the outlet of the flow domain and the lift coefficient value compared with xfoil.

Table (2): Comparison of C_l Between xfoil and Fluent Solver and $\Delta\dot{m}$

Mesh Type	Lift Coefficient	Net Mass Flux
C-Mesh	0.5137	-1.26×10^{-5} kgs^{-1}
C-Mesh 'R'	0.5182	-2.66×10^{-6} kgs^{-1}
Unstructured	0.5038	-5.27×10^{-8} kgs^{-1}
Unstructured 'R'	0.4969	-2.44×10^{-7} kgs^{-1}
xfoil	0.5105	-

For the 4 previous simulations, the net mass flux was very small it can be considered negligible, and the lift coefficient values were very similar to that of xfoil. Therefore, the TE errors shown in the above 4 graphs were due to TE modification. Because of this, another reliable source provided the 'NACA 4412' airfoil coordinates was used [10]. The coordinates obtained had no open TE, which eliminated TE issues, and provided a better pressure coefficient graph. It was very critical to have proper airfoil geometry since the same coordinates were used in the next 5 stages of the analysis.

The mesh chosen was the unstructured high-resolution mesh because the refinements can be tailored to the regions of interest, by having the mesh density increased closer to the airfoil and reduced further away, therefore reducing overall computational time. Additionally, refining the regions of interest captured the boundary layer effects and increase the accuracy of the results. The structured C-Mesh meshed the airfoil and the flow domain in a structured manner as seen in Figure (15); the more structured the mesh, the faster the convergence. However, the issue was that this type of mesh refines areas out of interest, leading to increased overall computational time, and the refinement cannot be tailored. Although the unstructured mesh had a considerably longer computational time, the accuracy it provided compensated the elongated computational time.

By using the unstructured high-resolution mesh to test the new 'NACA 4412' airfoil coordinates, the physical and the numerical setups are the same, 'Appendix (G)', and the pressure coefficient graph is shown below, the blue dots are xfoil and the orange dots are ANSYS Fluent.

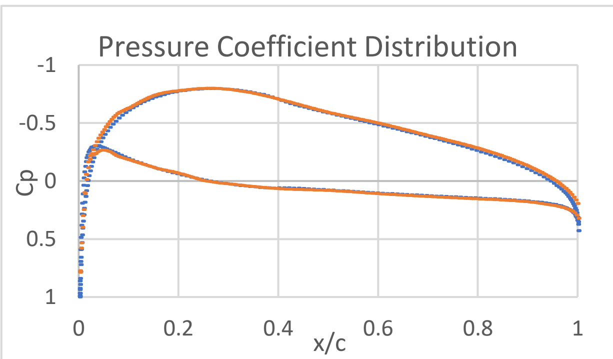

Graph (6): Pressure Coefficient Comparison Between xfoil and Fluent for New Airfoil

As shown in Graph (6), the TE follows the trend of the graph obtained from xfoil, further validating the mesh used. The net mass flux was $\Delta\dot{m} = -3.31\times10^{-8}$ kgs^{-1} which is very low and can be considered negligible, and the lift coefficient is 0.5111. Table (3) below shows the L^2 Norm comparison between the 5 tests and xfoil:

Table (3): L^2 Norm Comparison

Mesh Type	Cp^2 Sum	Points/Panels	Cp^2 ÷ Panels	% Difference from xfoil
C-Mesh	31.36466134	203	0.154505721	11.63%
C-Mesh 'R'	32.29985351	201	0.160695789	8.09%
Unstructured	79.12317178	502	0.15761588	9.85%
Unstructured 'R'	117.6318021	753	0.156217533	10.65%
Unstructured 'N'	82.55931374	502	0.164460784	5.93%
xfoil	52.44951745	300	0.174831725	-

Note: 'R' = Refined Mesh, 'N' = New Airfoil

Table (3) shows the difference between the pressure coefficient graphs of xfoil and ANSYS simulations which are shown in the 5th column. These percentages were obtained by summing the square of the pressure coefficient values, and then dividing them by the number of points or panels on the airfoil to obtain the average. This average was then divided by the average obtained from xfoil to find the difference between the pressure coefficient values. The one with the least percentage difference was the 'New Airfoil Coordinates' using the 'Unstructured Mesh' (row 6) which gave a difference of only 5.93%, this further validated the choice of the unstructured mesh. So, in further analysis, the new airfoil coordinates and high-resolution unstructured mesh were used.

6.2 2D Viscous Flow Around the Airfoil

This stage of the analysis tested for the best turbulent model which was used for the next 4 stages of the CFD analysis. Three turbulent models were tested:

'Spalart-Allmaras' model: a 1-equation model based on kinematic eddy viscosity and mixing length, where the mixing length defines the transport of the turbulent viscosity. This model is popular due to its robustness and fast implementation when modelling a certain flow [11].

'Realisable k-epsilon' model: a 2-equation model that solves for the turbulent kinetic energy 'k', and the rate of dissipation of kinetic energy, epsilon 'ε'. The 'Realisable' variation modifies the equation for ε, and it introduces the effect of the mean flow distortion on turbulent dissipation [11].

'SST k-omega' model: a 2-equation model that solves for the turbulent kinetic energy 'k', and the specific rate of dissipation of kinetic energy, omega 'ω'. It aims to model the near wall interactions with more accuracy than k-ε. The shear stress transport 'SST' modification gained popularity due to its ability to predict separation and reattachment better than k-ε and can solve for aerospace applications that are deemed too complex for the 'Spalart-Allmaras' model [11].

Each model was tested 3 times. The first time using a normal mesh which was of arbitrary refinement. The second mesh was the same mesh but refined by 25%, and the third mesh was refined by 50%. As seen in Figure (16), the highly dense area around the airfoil was refined, while the rest of the flow domain was left unchanged. The refinement percentages were done based on the cell size reduction and cell number increase in the regions of interest. Table (4) shows the number of cells that corresponds to the mesh refinement.

Table (4): Mesh Refinement and Number of Cells

Turbulent Model	Refinement	Number of Cells
Spalart-Allmaras	Normal	23148
	25%	35486
	50%	66803
Realizable k-epsilon	Normal	23148
	25%	35486
	50%	76257
SST k-omega	Normal	23148
	25%	35486
	50%	66803

The normal mesh for all three models, and the 25% refinement for the three models, have the same number of cells. However, the 'Realizable k-ε' had about 10000 more cells with the 50% refinement than the other two. The 'Realisable k-ε' at the 50% refinement could not converge due to the nature of the unstructured mesh, and the drastic size change when moving from the coarse to the refined area. Therefore, a small refinement was made to slightly reduce the average cell size of the mesh in the flow domain to obtain convergence. The dense mesh region was refined identically for all three models to maintain a fair comparison between the 3 turbulent models and eliminate any risk of numerical discretization errors.

Each model had the same physical and numerical setups for all 3 refinements as shown in Appendix (H). The numerical linearization errors were avoided by reducing the convergence absolute criteria for all residuals to 1×10^{-6}. The required Reynolds number was 70000, which dictated the velocity to be about $15.8ms^{-1}$ as calculated above. The airfoil had a chord length of 0.065m and was at $\alpha=9.5^{o}$. The best turbulent model was chosen based on having the closest lift, drag, and pressure coefficient to that of xfoil, the results are shown below. Note: The flow domain geometry was scaled down by 0.065 to match the airfoil to flow domain size ratio as done in the 1^{st} stage.

Table (5): Lift and Drag Coefficients Comparison

Turbulent Model	Refinement	Fluent C_l	Scaled C_l	Fluent C_d	Scaled C_d	L/D	Net Mass Flux (kgs^{-1})
Spalart-Allmaras	Normal	7.654×10^{-2}	1.178	2.853×10^{-3}	0.044	26.83	-8.29×10^{-9}
	25%	7.740×10^{-2}	1.191	2.719×10^{-3}	0.042	28.47	-1.11×10^{-8}
	50%	7.699×10^{-2}	1.184	2.709×10^{-3}	0.042	28.41	-6.64×10^{-9}
Realizable k-epsilon	Normal	8.508×10^{-2}	1.309	2.188×10^{-3}	0.034	26.69	-4.57×10^{-9}
	25%	8.524×10^{-2}	1.311	3.139×10^{-3}	0.048	27.16	1.20×10^{-9}
	50%	8.520×10^{-2}	1.311	3.012×10^{-3}	0.046	28.29	-1.35×10^{-9}
SST k-omega	Normal	7.674×10^{-2}	1.181	2.642×10^{-3}	0.041	29.04	-2.08×10^{-8}
	25%	7.653×10^{-2}	1.177	2.545×10^{-3}	0.039	30.07	-1.35×10^{-8}
	50%	7.689×10^{-2}	1.183	2.513×10^{-3}	0.037	30.60	-2.30×10^{-9}
xfoil	-	-	1.365	-	0.031	43.82	-

Before proceeding with any further analysis, the lift and drag coefficients obtained from ANSYS Fluent were scaled down by the chord length since it was a 2D flow. By dividing Fluent values of C_l and C_d by the chord length, the coefficient values were scaled up to the true values as shown in columns 4 and 6 in Table (5). This trend was seen in all 9 CFD simulations, where all the values were similar; however, they were scaled down. All 9 simulations had very similar Lift/Drag (L/D), and they were all somewhat close to that of xfoil. The values were trusted since both the numerical discretization and linearization errors were eliminated by the refined mesh, and by the reduced value of convergence absolute criteria for all residuals to 1×10^{-6} respectively. Moreover, mass was conserved since the net mass flux could be considered zero as shown in Table (5). Therefore, the coefficient values were scaled down because the reference point that ANSYS Fluent uses is the chord length and the span of the wing, whereas xfoil uses the normalized chord length.

Table (6): L^2 Norm Comparison

Turbulent Model	Refinement	Cp^2 Sum	Points/Panels	$Cp^2 \div$ Panels	% Difference from xfoil
Spalart-Allmaras	Normal	361.7613306	502	0.720640101	56.33%
	25%	461.6509847	629	0.733944332	55.53%
	50%	541.7955912	753	0.719516057	56.40%
Realizable k-epsilon	Normal	438.3716351	502	0.873250269	**47.09%**
	25%	546.7867185	629	0.86929526	**47.33%**
	50%	650.9419285	753	0.864464713	**47.62%**
SST k-omega	Normal	365.9374506	502	0.728959065	55.83%
	25%	454.4286633	629	0.722462104	56.22%
	50%	544.0486189	753	0.722508126	56.22%
xfoil	-	495.1118201	300	1.650372734	-

By looking at Tables (5) and (6), the 'Realisable k-ε' model provided the closest results to xfoil. It provided the closest values of the pressure distribution along the airfoil's surface, which was about 47.62% difference. Additionally, the values of the lift and drag coefficients of the model are 1.311 and 0.046 respectively, which are the closest to xfoil's values of C_l=1.365 and C_d=0.031. Therefore, the 'Realisable k-ε' was used in the following stages of analysis.

To ensure that ANSYS Fluent was only scaling the coefficient values without affecting other results as the lift force, a small analysis was done to just test the relationship between the lift force and the lift and drag coefficients against two different sizes of a 3D wing. Two wings of different sizes were tested at the same Reynolds number of 1000000 and had the same airfoil 'NACA 4412' at α=0°. The airfoil at Reynolds number of 1000000 was analysed using xfoil which resulted in C_l=0.4737 and C_d=0.0069. The velocity over both wings was found using Eq. (4). Air density and dynamic viscosity were set to $1.225 kgm^{-3}$ and 1.7965×10^{-5} $kgm^{-1}s^{-1}$ respectively. Thus, air velocity over the first wing of 1m chord length and 1m span was $14.67ms^{-1}$. And the velocity over the second wing of 0.5m chord length and 0.5m span was $29.33ms^{-1}$. However, by using Eq. (1) and (3), both wings resulted in the exact same lift force of 56.2N.

Afterwards, the analysis was done on ANSYS, both wings had the exact same analysis conditions using the 'Realisable k-ε' model and the results are shown in Table (7).

Table (7): Lift Force, Lift and Drag Coefficients Comparison

Wing	Lift Coefficient	Drag Coefficient	Lift/Drag	Lift Force	Net Mass Flux (kgs^{-1})
1m chord & span	0.435	0.017	25.3	57.3N	7.25×10^{-5}
0.5m chord & span	0.108	0.0043	25.0	57.1N	-2.93×10^{-5}
xfoil	0.474	0.0069	68.65	-	-

The residuals of Fluent solver never converged because of vortex shedding. This led to oscillations in the residuals in which the average trend line across these oscillations never reduced. A good measure for whether to trust ANSYS Fluent results is to look at the net mass flux, and the variation in C_l and C_d

values. The net mass flux was very small so mass was considered conserved as seen in Table (7). In addition, C_l and C_d values stabilized up to the 3rd to 4th decimal place.

The lift force matched the calculations and the C_l matched xfoil for the 1m wing chord and span. The lift also matched the calculations for the 0.5m wing chord and span. However, the C_l was scaled down by 4. Since L/D for both wings was the same, the lift coefficient of the 1m wing chord and span was divided by the lift coefficient value of the 0.5m wing chord and span, resulting in 4. This proved that ANSYS gives the right results; however, it scaled down the C_l and C_d values because the reference point that it used to calculate them was different from that of xfoil.

Moving on, a separation bubble occurred on the airfoil due to having very low Reynolds flow. Since Reynolds number is 70000, xfoil showed a separation bubble between 0.02-0.04m as shown in Graph (7). At about 0.02m in Graph (7), the value of the pressure coefficient became relatively constant, indicating that the flow separated. However, the pressure coefficient value increased sharply at about 0.026m, indicating reattachment. The reattachment occurred due to the flow transitioning and reenergising itself. This phenomenon can be also seen in Graph (8): the friction coefficient has a negative value between 0.2-0.4 x/c which suggests that there is a separation bubble. In Graph (8), the blue line resembles the friction coefficient distribution over the top surface of the airfoil, and the orange line resemble the friction coefficient distribution over the bottom surface of the same airfoil.

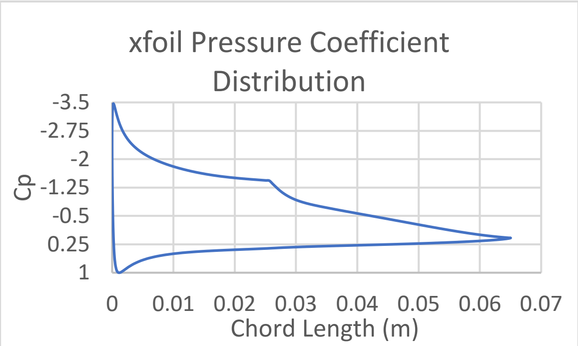

Graph (7): Pressure Coefficient Distribution Along the Airfoil's Surface

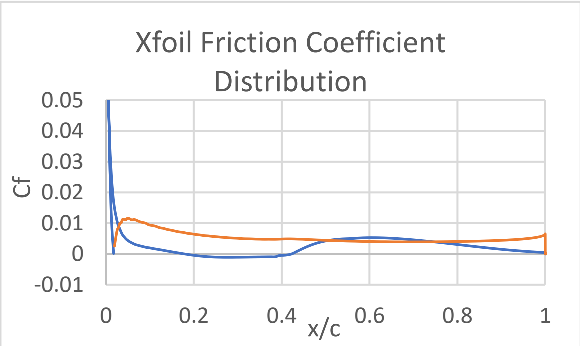

Graph (8): Friction Coefficient Distribution Along the Airfoil's Surface

Although Reynolds number was very low for the 9 simulations, they showed little to no separation. The 'SST k-omega' turbulent model was the only model to visibly show the separation bubble as seen in Graph (9); however, when compared to xfoil, it was minimal. The 'Spalart-Allmaras' and 'Realisable k-epsilon' models showed no sign of a separation bubble as seen in Graphs (10) and (11).

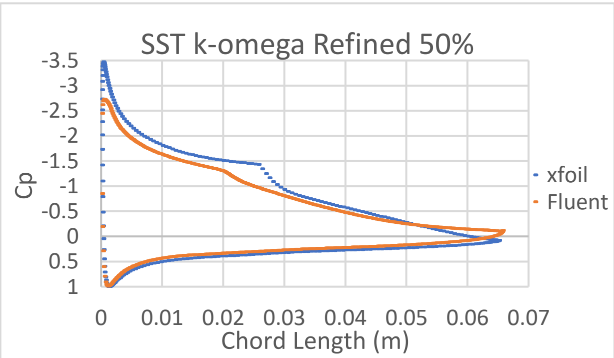

Graph (9): Pressure Coefficient Comparison Between xfoil and 'SST k-omega' Refined 50%

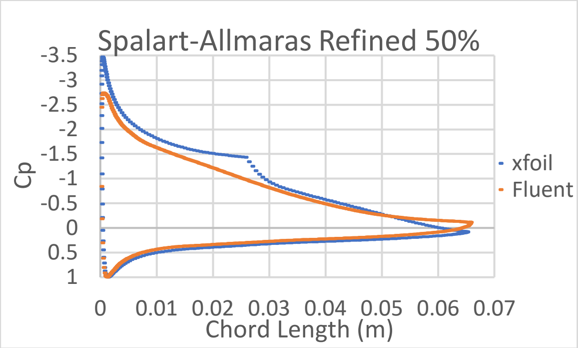

Graph (10): Pressure Coefficient Comparison Between xfoil and 'Spalart-Allmaras' Refined 50%

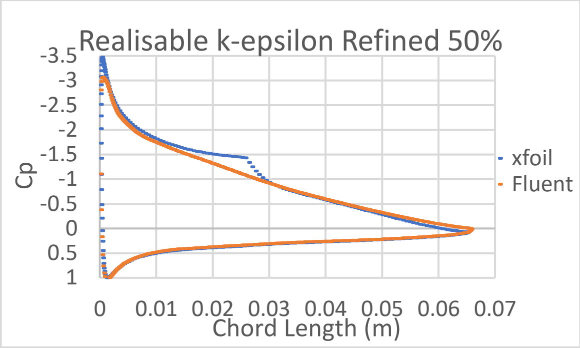

Graph (11): Pressure Coefficient Comparison Between xfoil and 'Realizable k-epsilon' Refined 50%

The friction coefficient distribution along the surface of the chosen model, 'Realisable k-ε,' as shown in Graph (12), shows a tiny separation bubble at about 0.056m across the chord (0.86 x/c), which does not match xfoil.

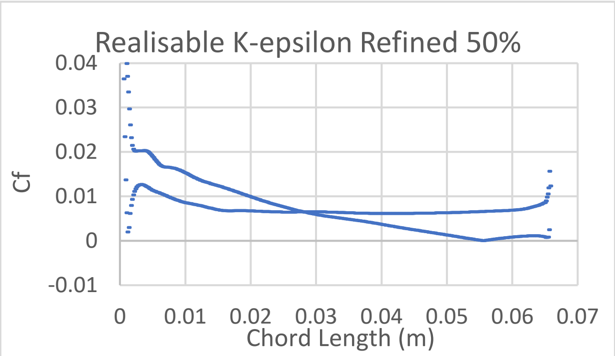

Graph (12): Friction Coefficient Distribution Along the Surface for 'Realizable k-epsilon' Refined 50%

In this case, ANSYS values are trusted over xfoil, because xfoil uses the panel method to solve and its values can be trusted so long as there is no separation bubble or flow detachment. Xfoil idealises the flow, even if it is viscous and there is a separation bubble or flow separation. It assumes perfect flow, and it neglects the turbulent effects and idealise the turbulent boundary layer. It always assumes that the turbulent boundary layer starts from the same place irrespective of the conditions of the flow. In reality, the point where the turbulent boundary layer starts is difficult to locate, it oscillates back and forth depending on the flow characteristics.

ANSYS is more trustworthy in the case of separation bubble and flow detachment because it uses a full CFD model. It considers factors such as turbulent effects, air viscosity, density, temperature and other imperfections in the free stream that xfoil neglects. Xfoil can be trusted for simple flows only. Xfoil is very idealised, hence the very high C_l and very low C_d values as seen in Table (5), and the very sharp perfectly positioned separation bubble as seen in Graph (7). ANSYS, being more realistic, showed no separation bubble as it appeared that the flow had enough energy to avoid any separation bubbles, and so, the C_l was less than that of xfoil and the C_d was a bit higher.

The 'Realisable k-ε' model was the perfect choice to be used for later stages. It is very robust and showed very similar results to xfoil, and very similar results to the theoretical calculations that were done to test the 3D wing as shown in Table (7). So far, the unstructured high-resolution mesh and the 'Realisable k-ε' model were used for the rest of the stages. The analysis that was done in the coming stages validated the design and the shape of the vehicle, since the type of mesh and the physical and numerical setups have been chosen.

6.3 3D Flow Around a Straight Wing

This stage of the analysis simulated a flow over a simple 3D straight wing. The lift force obtained acted as a reference point to which the 3D circular wing's lift force was compared with. This stage and the next tested the wing as if it was being tested in a wind tunnel with a clean freestream air flowing over the wing. The next stage of analysis will have a clean, freestream, radial flow of air flowing over the circular wing. This helped to get the true performance for both wings and to understand what effects the addition of a duct added.

For simplification, only 10° of the full 360° circular wing was tested to reduce the computational time, and to have a finer mesh on the test portion. The area obtained from this portion will be the same for the straight wing. The LE radius of the circular wing is 0.135m, and the TE radius is 0.2m. This left the wing chord to be 0.065m. For a 10° portion, the wing area is:

$$\frac{10}{360} \times (\pi(0.2)^2 - \pi(0.135)^2) = \underline{1900.227223\times10^{-6}m^2}$$

The area of the straight wing is as simple as multiplying the chord length by the span. This left the span to be 29.23426497×10^{-3}m, with the chord length fixated at 0.065m. The flow domain for the straight wing was designed to be large enough so that the boundaries would not affect the behaviour of the wing. The actual air velocity over the wing, as calculated earlier, was $15.7402ms^{-1}$ which corresponds to a Reynolds number of 69764.38. For simplicity, Reynolds number was rounded up to 70000 and this resulted in an air velocity of approximately $15.8ms^{-1}$. The lift coefficient was 1.365 at $\alpha=9.5°$, the air velocity, and the wing area are the same as what has been calculated earlier. Eq. (1) and (3) were used to find the lift force produced by this wing segment. This produced a lift force of about L=0.357N, which if multiplied by 36 to account for the whole wing, the overall lift force is 12.85N.

The details of the physical and numerical setups are available in Appendix (I). The numerical linearization errors were avoided by reducing the convergence absolute criteria for all Residuals to 1×10^{-6}. After running the simulation, a grid independence study was performed to reduce the discretization error. The results from the CFD simulations are provided in Table (8) below:

Table (8): Grid Independence Study for the Straight Wing

3D Straight Wing	Number of Cells	Lift Force	Drag Force	Lift/Drag	Net Mass Flux (kgs^{-1})
Normal	646838	0.366N	0.021N	17.517	4.63×10^{-9}
Refined	2383622	0.371N	0.020N	18.293	-1.28×10^{-9}

Because the change in the lift force was very small, within 5% range, there was no need for a third mesh refinement. The lift force for the normal and refined meshes were about 2.81% and 4.21% higher than the lift force calculated earlier of 0.357N, respectively. The drag force was considerably low which provided an acceptable L/D ratio. As seen in Figure (17), the wing had no separation, and the flow was running smoothly, thus producing the correct lift force. This further validates the 'Realisable k-ε' model, which had an acceptable error tolerance, at least for this design stage of the vehicle's design life cycle. At this point, the lift force obtained will act as a reference point for the next stage.

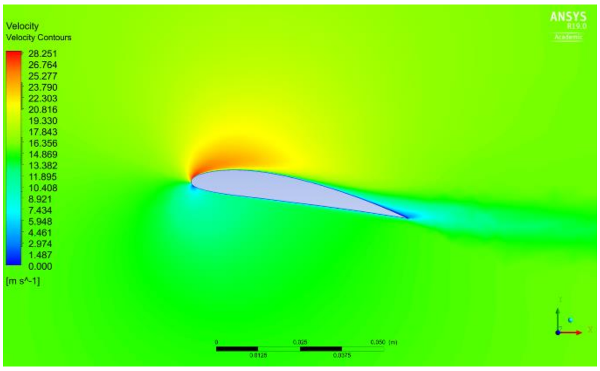

Figure (17): Velocity Contours over the Refined Straight Wing

6.4 3D Flow Around a Circular Wing

In this stage, the 10° circular portion of the wing was tested and compared to the lift force values of the previous stage. The flow domain looks like a 10° wedge of a cylinder as seen in Figure (18).

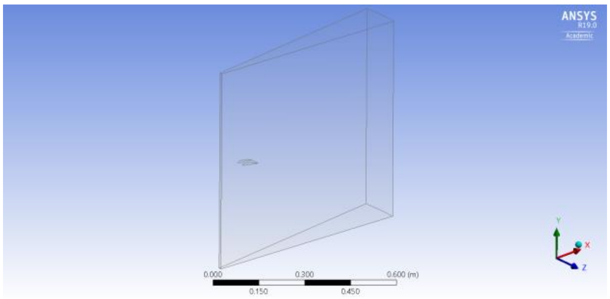

Figure (18): Circular Wing 10° Flow Domain Portion

The radial flow slowed down as it moves outwards, making the CFD simulation challenging. To reduce possible errors, the boundaries of the flow domain were made large enough to avoid potential boundary effects that could hinder the wing's performance. The top and bottom surfaces of the flow domain were adjusted to behave as a wall allowing slip condition (zero shear). It was not possible to set them as velocity boundaries since the velocity slows down when moving down stream. The sidewalls of the wedge were specified as symmetric walls, and they behaved as if the model extends to 360°. They imposed no effect on the part of the wing that is close to the wall.

The inlet velocity was unlike the previous stage, because the inlet of the flow domain was at a radius of 0.05m from the centreline, and the average velocity over the wing (can be assumed at mid-chord) was 15.8ms^{-1}. By using Eq. (7), the velocity at the inlet was 52.93ms^{-1}, and by the time the flow reached the wing, the speed will have reduced to reach the desired air velocity and Reynolds number. The wing was at an angle of 9.5° with a C_l=1.365, and mathematically should produce L=0.357N. This test was identical to the previous stage except that the wing is circular. The numerical and physical setups are available in Appendix (J). The numerical linearization errors were avoided by reducing the convergence absolute criteria for all Residuals to 1×10^{-6}. The results of the simulation are provided in Table (9) below.

Table (9): Grid Independence Study for the Circular Wing

3D Circular Wing	Number of Cells	Lift Force	Drag Force	Lift/Drag	Net Mass Flux (kgs^{-1})
Normal	817280	0.219N	7.214×10^{-3}	30.336	-1.02×10^{-7}
Refined	3555098	0.208N	2.728×10^{-3}	76.206	2.32×10^{-5}

As shown in Table (9), the lift force obtained from the normal and refined meshes was about 61.34% and 58.26% respectively of the theoretical 0.357N. This loss in lift was due to the slowing air since it is moving radially outwards, which also caused partial flow detachment due to a low Reynolds number, as seen in Figure (19).

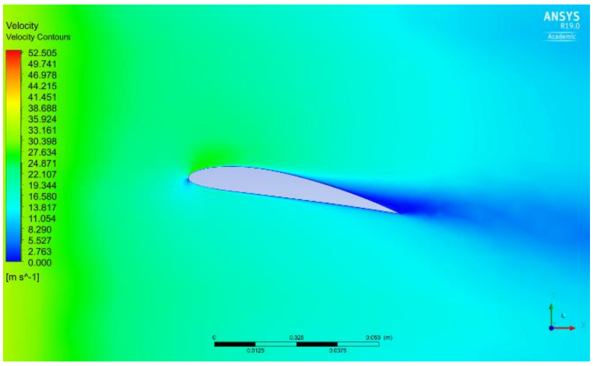

Figure (19): Velocity Contours over the Refined Circular Wing

The partial flow detachment was due to flow slowing down which in turns reduced Reynolds number. The best way to avoid flow detachment or partial separation is to increase Reynolds number. This can be done in two ways: increasing the chord length and so, the wing area, or increasing flow velocity. In this case, increasing the chord length would not be helpful as the flow is already partially detached, and Reynolds number at the point of detachment is low enough to allow the flow to attach. There is no reason to use extra chord length because the flow will never reattach as long as it is moving radially. However, increasing the flow velocity would provide enough energy to the flow to reattach it.

To test this theory, another CFD simulation was done, but with an increased Reynolds number due to increasing the flow velocity. Reynolds number was increased to around 100000. By using Eq. (4), the average velocity over the wing (at mid-chord) was 23.135ms^{-1}, producing a Reynolds number of about 103000. By using xflr5 at Re=103000, the highest L/D value was 56.557 which corresponded to an AoA of 9^{o}, this gave a lift coefficient of C_l=1.353. By performing Eq. (1) and (3), the new theoretical lift force was 0.759N.

The physical and numerical setups are available in Appendix (K). The only difference between this analysis and the previous analysis was the inlet velocity. Since the average velocity over the wing was 23.135ms^{-1}, by using Eq. (7), the velocity at the inlet of the flow domain was 77.502ms^{-1} since the inlet radius is 0.05m from the centre. The numerical linearization errors were avoided by reducing the convergence absolute criteria for all Residuals to 1×10^{-6}. The results of the simulation are provided in Table (10) below.

Table (10): Grid Independence Study for the Circular Wing at Re=103000

3D New Circular Wing	Number of Cells	Lift Force	Drag Force	Lift/Drag	Net Mass Flux (kgs^{-1})
Normal	817332	0.462	9.405×10^{-3}	49.123	1.29×10^{-4}
Refined	1688152	0.442	11.199×10^{-3}	39.469	1.43×10^{-6}

As shown in the table above, the lift force obtained from the normal and refined meshes was about 60.87% and 58.23% respectively of the theoretical 0.759N. The detachment was less than the previous simulation, as seen in Figure (20). The results were consistent with the previous test which gave about 61.34% and 58.26% respectively from their theoretical lift force of 0.357N. It was evident that this is the wings performance due to its circular design. As a total of 4 simulations so far gave similar results, this served enough evidence at this stage to prove that the circular wing by itself has about 58% lift of its straight counterpart wing.

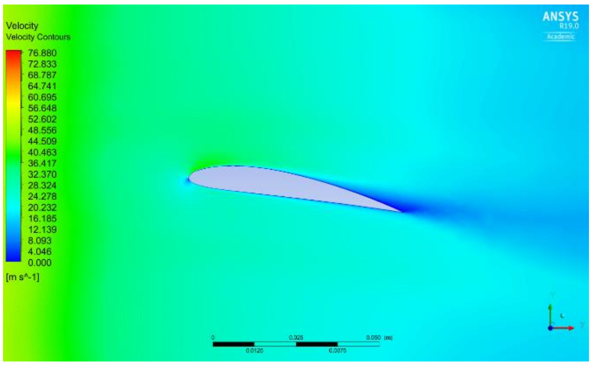

Figure (20): Velocity Contours over the Refined Circular Wing at Re=103000

To solve the partial flow detachment issue, there were three potential solutions:

1) To reduce the AoA, which would reduce the lift force but could avoid flow detachment.
2) To increase the radius of the exit duct and the wing. The relationship between the radius and the velocity is a power relation (Appendix (E)). At some point far from the centre, the rate of decrease in velocity will reduce enough as the radius increases. This means that the change in velocity between the LE and the TE will be small, thus avoiding the sudden reduction in Reynolds number and flow detachment. However, the vehicle will become too large and heavy, thus it is not practical.
3) To greatly increase the power input of the electric motor to move air faster. This will increase Reynolds number and potentially avoid detachment. However, this solution is not feasible at this scale of the project. The power required to increase Reynolds to a high enough value to avoid any separation will be very high.

The first solution was chosen to be tested to avoid partial flow detachment. The wing's average velocity was 23.135ms^{-1} from the previous simulation, and by using Eq. (4), it gave a Reynolds number of 103000. The lift force that was produced was limited to 0.357N, and after using Eq. (1) and (3), the lift coefficient was C_l=0.6368. By using xfoil, the AoA that corresponded to this C_l value was α=1.6222°. The numerical and physical setups are available in Appendix (K). The numerical linearization errors were avoided by reducing the convergence absolute criteria for all Residuals to 1×10^{-6}, the results are shown in Table (11).

Table (11): Grid Independence Study for the Circular Wing at α=1.6222°

3D New Circular Wing	Number of Cells	Lift Force	Drag Force	Lift/Drag	Net Mass Flux (kgs^{-1})
Normal	816282	0.161	0.010	16.144	-1.34×10^{-6}
Refined	1699259	0.187	0.008	22.280	4.02×10^{-5}
Extra Refined	3557485	0.247	0.007	33.677	7.72×10^{-7}
Super Refined	6879041	0.257	0.006	44.370	4.35×10^{-6}

As seen in the table above, the performance of the wing was improved after each refinement which resulted in 45.10%, 52.38%, 69.19%, and 71.99% for the normal, refined, extra refined, and super refined meshes respectively of the theoretical lift force of 0.357N. The wings performance was also improved in terms of the lift force. It increased by about 13% from previous simulations, and this is a result of eliminating the partial flow detachment by reducing the AoA as seen in Figure (21).

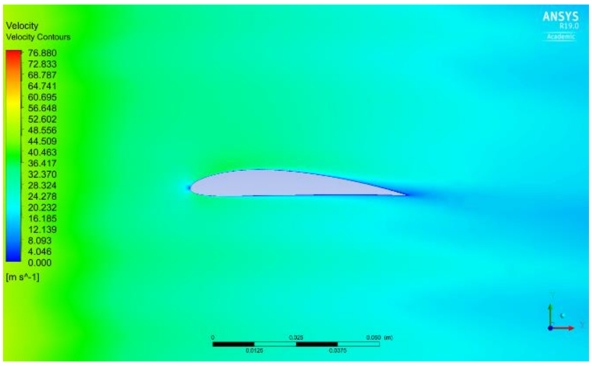

Figure (21): Velocity Contours over the Super Refined Circular Wing at α=1.6222°

6.5 3D Flow Around a Straight Wing with a Duct

At this stage, a small portion of the straight wing with a span of 29.23426497×10^{-3}m was tested; however, a duct was added in front of the wing to study what changes occurred in the wing's performance. The span corresponds to the same wing area a 10° portion of the circular wing. As mentioned in the 'Wing Positioning' section, the wing's position obtained is the same for this CFD test. The duct had a height of 0.01m, the wing's LE is 0.01m away from the duct, and the wing of chord length of 0.065m is at an angle of 9.5° with a C_l=1.365. Again, the test was conducted at a Reynolds number of 70000 with an air velocity of 15.8ms^{-1}. By using Eq. (1), the theoretical lift force was 0.357N.

In the simulation, the duct had a constant height in this case, due to the flow moving straight. However, the duct had the same length of that for the circular wing flow, as it was critical to capture any effects the boundary layer may have imposed. If the duct was of any other length, the results could not be comparable with the next stage. The flow domain can be seen in Figure (22) below.

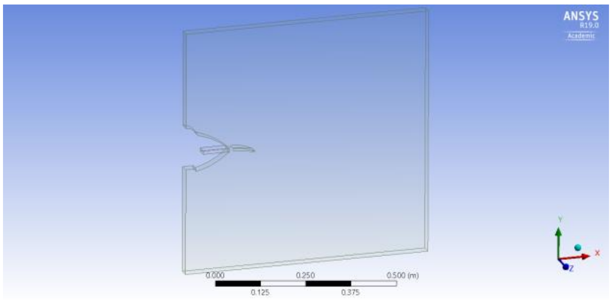

Figure (22): Straight Wing Flow Domain

The physical and numerical setups are available in Appendix (L). The numerical linearization errors were avoided by reducing the convergence absolute criteria for all Residuals to 1×10^{-6}. The results of the simulation are provided in Table (12) below:

Table (12): Grid Independence Study for the Ducted Straight Wing

3D New Circular Wing	Number of Cells	Lift Force	Drag Force	Lift/Drag	Net Mass Flux (kgs^{-1})
Normal	1293075	0.024	0.011	2.169	-1.79×10^{-8}
Refined	2400595	0.024	0.011	2.224	-7.30×10^{-8}

As shown in Table (12), the lift forces obtained from both the normal and refined meshes were nearly identical, and about 6.72% of the theoretical lift force obtained of 0.357N. The straight wing segment had barely produced any lift, which could be due to few reasons: as shown in Figure (23), the air velocity at the top and bottom of the wing was approximately the same, prohibiting the wing from producing enough lift. This occurred due to the air speeding up within the duct, due to the boundary layer effect and mass conservation.

For a finite Reynolds number, the boundary layer has a thickness. This effect is missed by the 'Classical Boundary Layer Theory' which assumes that the outer flow outside the boundary layer is inviscid. This is true if the boundary layer is infinitely thin and Reynolds number approaches infinity [12]. For a finite Reynolds number, the boundary layer has a thickness which displaces some of the outer flow causing the flow to speed up [12]. As the flow proceeded within the duct, the boundary layer increased in thickness which ate up more of the flow area. Since the boundary layer retarded the flow, this reduced the mass flow close to the wall. Because mass is conserved, the flow compensated for this issue by slightly speeding up as seen in Figure (23) by the darker contours within the duct. Since the flow increased in speed, Reynolds number increased over the wing, avoiding flow detachment. While the natural speeding up of the air sounds advantageous, the boundary effects confined the flow to a smaller area.

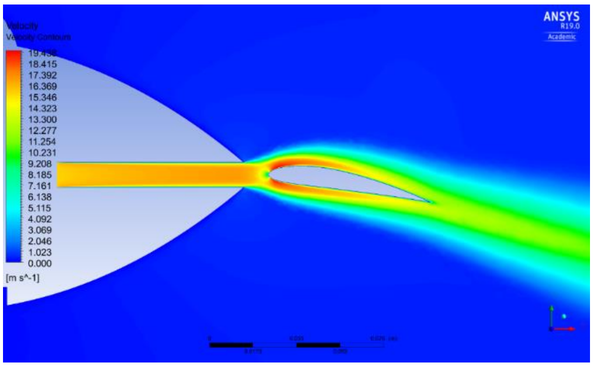

Figure (23): Velocity Contours Over the Refined Ducted Straight Wing

The decrease in flow area confined and increased the airflow velocity which affected the behaviour of the wing. The increased airflow speed had considerably more kinetic energy than the stationary air around it, thus it was able to displace that air and move around the wing without allowing the wing's geometry to play its role to create pressure unevenness. And this probably was the reason behind the poor performance of the wing.

6.6 3D Flow Around a Circular Wing with a Duct

For this final section, 10^o of the full 360^o wing was tested with the same exact test condition used in stage (5). The wing's LE was placed 0.01m away from the duct exit which had a radius of 0.125m. The wing had a chord length of 0.065m at an angle of attack 9.5^o and C_l=1.365. The Reynolds number was at 70000 with an average air velocity of 15.8ms^{-1}. By using Eq. (7), the velocity at the duct exit was 21.172ms^{-1}. For the radial flow to achieve a 15.8ms^{-1} averaged flow over the wing, the velocity at the inlet of the duct must be very high. The duct had a length of 0.075m, and the inlet was located at a radius of 0.05m from the centre. By using Eq. (7), the velocity at the inlet of the duct was found to be 52.936ms^{-1}. This velocity was very high and would require a lot of energy for the motor to produce this air velocity. Therefore, the duct was designed in a fashion to maintain the same air velocity through it.

6.6.1 Duct Design

At this stage of the design, it was crucial to have a properly designed air duct since it was the only mean that transported air directly from the centrifugal fan to the wing. The duct was designed to just maintain the airspeed throughout its length. As the air moves radially outward, if the duct height is maintained constant, air will slow down. Therefore, the duct was designed to have the same flow area at any cylindrical cross-section throughout its radial length. This created a diverging duct, and so air velocity was maintained.

The process started by finding the flow area at a known point. In this case, the known point is the outlet of the duct: it had a radius of 0.125m and the duct exit height at that point was 0.01m. The flow area was found to be $7.854\times10^{-3}m^2$. The duct length was then divided into segments of 0.005m, then calculated the height to match the area previously found. The values are provided in the following table, and the duct design is shown in Figure (24).

Table (13): Duct Measurements

Radius(m)	0.050	0.055	0.060	0.065	0.070	0.075	0.080	0.085
Height(m)	1/40	1/44	1/48	1/52	1/56	1/60	1/64	1/68
Radius(m)	0.090	0.095	0.10	0.105	0.110	0.115	0.120	0.0125
Height(m)	1/72	1/76	1/80	1/84	1/88	1/92	1/96	1/100

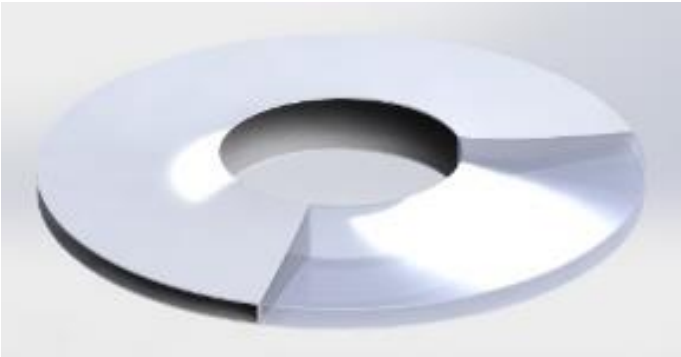

Figure (24): Duct Design

Figure (24) shows the shape of the radial air duct, with the 120° portion set to be transparent so the wall contours can be seen. The air travels from the centre of the duct radially towards the outer opening. This way, the motor would produce an air velocity of $21.172ms^{-1}$, and as soon as the air exits the duct, it will start slowing down. When the flow reaches the wing, the velocity would be $15.8ms^{-1}$, thus satisfying the design conditions.

The theoretical lift force from the 10° portion was 0.357N by using Eq. (1) and (3). The physical and numerical setups are available in Appendix (M). The numerical linearization errors were avoided by reducing the convergence absolute criteria for all Residuals to 1×10^{-6}. The results of the simulation are provided in Table (14) below:

Table (14): Grid Independence Study for the Ducted Circular Wing

3D New Circular Wing	Number of Cells	Lift Force	Drag Force	Lift/Drag	Net Mass Flux (kgs^{-1})
Normal	1518572	0.0381	0.0163	2.3422	-2.81×10^{-8}
Refined	2610418	0.0385	0.0161	2.3823	2.19×10^{-7}

As shown in the table above, the lift forces obtained from the normal and refined meshes were 10.67% and 10.78% of the theoretical lift of 0.357N. As the mesh was refined, the lift force was slightly enhanced. While the wing producing a low lift, it showed an improvement from the previous stage which produced 6.72% of the theoretical 0.357N. This simulation proved that the reduced lift value was due to the boundary layer effects. The height of the duct at its exit is the same as the previous stage: 0.01m indicating that the wing was facing the same exact issues. This is shown in Figure (25).

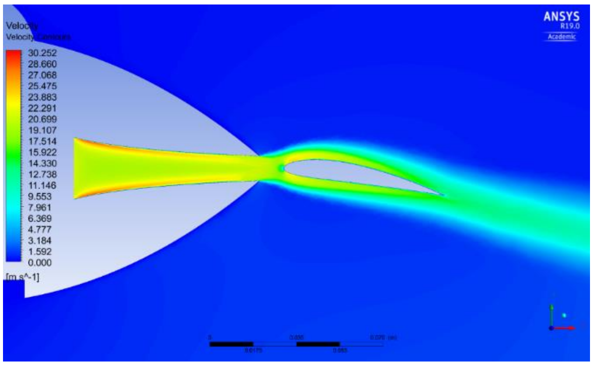

Figure (25): Velocity Contours Over the Refined Ducted Circular Wing

The circular wing still produced more lift force than the straight wing segment. Although both wings have the same wing area, flow domains, physical and numerical setups, and mesh; the circular wing produced more lift. The reason behind this phenomenon is that the boundary layer effects were reduced due to the circular geometry. As the flow exited the duct for the straight wing, it was filled with vortices and eddies. The straight wing encountered all these disturbances and could not provide sufficient lift as aforementioned. However, in the circular wing case, as soon as the flow exited the duct, the height of the flow is assumed constant as shown in Figure (14). This suddenly led to the reduction of the flow's velocity due to the air flowing through larger and larger areas. In this case, air slightly expanded and diffused, and the action of the air slowing due to its radial motion dampened the flow disturbances formed from the duct and increased the flow quality, thus the slight increase in lift. Additionally, the velocity throughout the duct was constant which proves that the duct was performing its intended job.

This problem has two potential solutions: to increase the duct height and to slightly push the wing further away from the duct. Increasing duct height would reduce the boundary layer effect and allow the wing to interact more with the better-quality air that comes out from centre of the duct. However, there is a limit to how much the duct height could be increased, as a very large duct inlet is unpractical. Therefore, the height of the duct at its exit was increased from 0.01m to 0.02m, and the rest of the measurements are provided in the tale below.

Table (15): New Duct Measurements

Radius(m)	0.050	0.055	0.060	0.065	0.070	0.075	0.080	0.085
Height(m)	1/20	1/22	1/24	1/26	1/28	1/30	1/32	1/34
Radius(m)	0.090	0.095	0.10	0.105	0.110	0.115	0.120	0.0125
Height(m)	1/36	1/38	1/40	1/42	1/44	1/46	1/48	1/50

Pushing the wing away from the duct exit will give more room for the air to diffuse and gain some quality to enhance the lift force. But, this will require slightly faster airflow at the duct exit since the wing is slightly further. The wing was shifted by further 0.01m away from the duct exit while maintaining the same chord length of 0.065m. This increased the LE radius from 0.135m to 0.145m. To maintain the same Reynolds number of 70000 and average velocity (velocity at mid-chord) of 15.8ms^{-1}, the velocity at the duct exit was set at 22.44ms^{-1}. This velocity was found by using Eq. (7), where the new mid-chord radius was 0.1775m, and the duct exit radius remained at 0.125m. Also, the shifting resulted in a slight increase in the wing area since the TE radius increased from 0.2m to 0.21m. The new wing area is as follows:

$$\frac{10}{360} \times (\pi(0.21)^2 - \pi(0.145)^2) = \underline{2013.673624\times10^{-6}m^2}$$

The lift coefficient remained 1.365 at α=9.5°, by using Eq. (1) and (3). The theoretical lift force for the 10° circular wing portion was 0.378N. The physical and numerical setups are available in Appendix (M). The numerical linearization errors were avoided by reducing the convergence absolute criteria for all Residuals to 1×10^{-6}. The simulation results are provided in Table (16):

Table (16): Grid Independence Study for the New Ducted Circular Wing

3D New Circular Wing	Number of Cells	Lift Force	Drag Force	Lift/Drag	Net Mass Flux (kgs^{-1})
Normal	1572848	0.0930	0.0245	3.8021	6.93×10^{-9}
Refined	2696621	0.0933	0.0242	3.8579	-3.37×10^{-8}

As shown in the table above, the lift force produced from the normal and refined meshes were 24.60% and 24.68% respectively of the theoretical lift force of 0.378N. By increasing the duct height and pushing the wing slightly further away from the duct, the lift force increased by about 14.5% from the previous simulation. The improvements can be seen in Figure (26). The wing contacted cleaner air as shown by the yellow contours that extended along the duct surface and moving above and below the wing. The cleaner air in this case is represented by the green contours. Also, there was no flow detachment due to slight increase in the flow velocity, resulting from the boundary layer effects as mentioned in the previous stage.

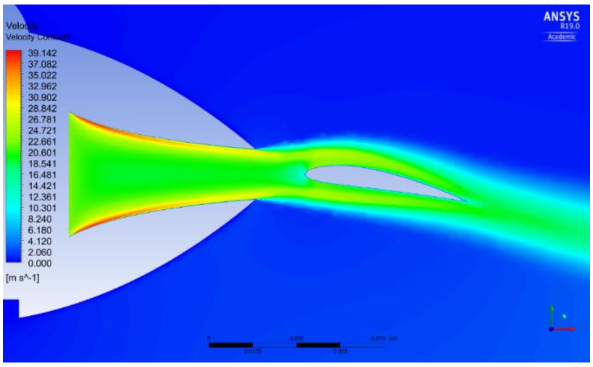

Figure (26): Velocity Contours Over the New Refined Ducted Circular Wing

Finally, an important comparison was made between the lift performance of the circular wing in the final simulation and a straight rectangular conventional wing with the same chord and wing area. Only the final simulation was used for this comparison because its geometry was used in the final 3D printed model. The lift force calculations of the rectangular straight wing accounted for all the realistic effects including downwash and tip vortices. These lift force calculations were based on the same flow environment the circular wing had, and a Reynolds number of 70000, which lead to a flow speed of $15.8ms^{-1}$ over the wing. The following equations were used to find the lift force.

$$L = \frac{1}{2}\rho V^2 C_L A \qquad \text{Eq. (1)}$$

Where C_L is the 3D lift coefficient and can be found using the following equation:

$$C_L = a(\alpha - \alpha_{L=0}) \qquad \text{Eq. (10)}$$

Where 'a' is the slope of '$C_L\ vs.\ \alpha$' curve for a finite wing, 'α' is the chosen angle of attack, and '$\alpha_{L=0}$' is the angle of attack at zero lift force. 'a' can be found by using the following equation:

$$a = \frac{a_o}{1+\left(\frac{a_o}{\pi.AR}\right)(1+\tau)} \qquad \text{Eq. (11)}$$

Where 'a_o' is the slope of 'C_l $vs.\alpha$' curve for an infinite wing, 'AR' is the wing's aspect ratio, and 'τ' is a function of the Fourier Coefficient (A_n) where values of 'τ' were calculated first by 'Glauert' in the early 1920s, and usually range between 0.05-0.25 [13]. It can be assumed that 'τ' is equal to 'δ' [14], where 'δ' is the induced drag factor. To find 'a_o', the average of three sections of the same slope were calculated since the curve was not perfectly straight, by using xfoil for 'NACA 4412':

For 'a_{o1}' ➔ α_2 = 8.5°, C_{l2} = 1.292 and α_1 = 2°, C_{l1} = 0.59 ➔ a_{o1} = 6.188

For 'a_{o2}' ➔ α_2 = 2°, C_{l2} =0.59 and α_1 = -3°, C_{l1} = -0.135 ➔ a_{o2} = 8.303

For 'a_{o3}' ➔ α_2 = 8.5°, C_{l2} =1.292 and α_1 = -3°, C_{l1} = -0.135 ➔ a_{o3} = 7.11

Therefore: $a_o = \frac{a_{o1}+a_{o2}+a_{o3}}{3} = \frac{6.188+8.303+7.11}{3} = \underline{7.202}$

In terms of the aspect ratio, the area of the circular wing was: $\pi(0.21^2\text{-}0.145^2) = 0.0724923\text{m}^2$, since the chord of the straight wing is 0.065m, then the span is 1.115m. Therefore, the aspect ratio was:

$$\text{AR} = \frac{S^2}{A} = \frac{S^2}{SC} = \frac{S}{C} = \frac{1.115}{0.065} = \underline{17.158}$$

Finally, for 'τ', since 'τ = δ', at an aspect ratio of 17.158 and taper ratio of 1, δ = τ = 0.17 [15], which was within the range as stated before. Thus, by using Eq. (11) the slope of a finite wing is:

$$a = \frac{7.202}{1+\left(\frac{7.202}{\pi\times17.158}\right)(1+0.17)} = \underline{6.23\text{rad}^{-1}} \quad ➔ \quad \underline{0.1087\text{deg}^{-1}}$$

Given that the zero-lift angle is -2.22° and the operating angle is 9.5°. By using Eq. (10), the 3D lift coefficient is:

$$C_L = 0.1087(9.5\text{-}(\text{-}2.22)) = \underline{1.274}$$

Finally, by using Eq. (1), the lift force is:

$$L = \frac{1}{2} \times 1.225 \times 15.8^2 \times 1.274 \times 0.0724923 = \underline{14.12\text{N}}$$

The 10° portion of the circular wing with the duct produced 0.0933N of force, so the whole wing will produce 0.0933 × 36 = <u>3.36N,</u> which is about **<u>23.8%</u>** of what the rectangular wing produced. The result is very similar to the comparison found earlier of 24.68%. This proved the validity of Eq. (3). Although it should be used for maximum lift coefficients to estimate the 3D lift coefficient, the argument was that the lift coefficient used of C_l = 1.365 was high enough which could validate the equation. To further prove this:

Eq. (3) gave $\frac{C_L}{C_l} = \underline{0.9}$

Eq. (11) and (10) gave $\frac{C_L}{C_l} = \underline{0.93}$

This proved that all the previous calculation were accurate considering this section as a first performance estimation for such a vehicle.

7. Centrifugal Fan Design

A centrifugal fan was designed to match the previous geometrical constraints that were applied to enhance the flow around the wing in the previous section. The centrifugal fan dimension constraints were a radius of 0.05m and a blade height of 0.05m. Several choices were considered to find the appropriate tool to deliver air efficiently, including an axial fan, a radial impeller, and a centrifugal fan, as shown in Figures (27), (28), and (29).

Figure (27): Axial Fan

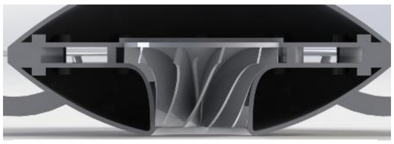

Figure (28): Radial Impeller

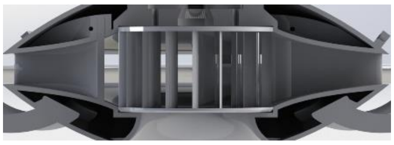

Figure (29): Centrifugal Fan

The axial fan was not a viable option. The air is sucked from below and must be turned at a 90^o angle to head towards the wing. The fan would have created flow unevenness, in addition to vortices blocking the flow and creating unnecessary pressure at the regions shown in Figure (30). Even smoothing out the duct to obtain a more regular air flow as shown in Figure (31), would not be sufficient.

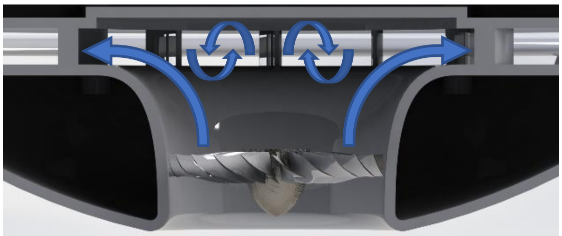

Figure (30): Pressure Unevenness and Vorticities

Figure (31): Smoothed Out Flow Path

The second option was the radial impeller, seen in Figure (28). Radial impellers are designed to turn the flow at a certain angle, commonly 90^o. Therefore, it does a better job at turning the flow with higher efficiency than the axial fan; however, the design constraints limit the impeller's performance. Radial impellers spin at high speeds: they speed up air while increasing dynamic pressure, and then the kinetic energy is turned into static pressure by either using veined or vein-less diffuser. As shown in Figure (28), the impeller's dimensions are not proportional, as the outlet area is too large. This will slow the flow rather than speed it up, acting as a turbine in this case. Additionally, the vehicle requires fast airflow, not pressure, and therefore, the radial impeller cannot perform this job properly.

The final option was the centrifugal fan. This device turns the flow efficiently and can deliver a range of airflow velocities at good efficiencies. After calculation trial and error, it appeared that the centrifugal fan can take any shape, radius, or height, and then the blades can be designed accordingly to match the flow requirements. The design parameters and calculations including the velocity triangles of the centrifugal fan which are shown below.

<u>Design Parameters:</u>

- Inner Blade Radius (r_1): **0.035m**
- Outer Blade Radius (r_2): **0.05m**
- Blade Height (h): **0.05m**
- Rotation (N): **4000rpm**
- Mass Flow Rate ($\dot{m}$): **0.431719 kgs^{-1}**
- Volumetric Flow Rate ($\dot{Q}$): **0.352424 m^{3}s^{-1}**

There are some parameters that this centrifugal fan must confine to so that the design works efficiently. As the centrifugal fan is adding kinetic energy to the flow, the absolute velocity at the outlet (V_2) must be greater than the absolute velocity at the inlet (V_1). Moreover, the flow outlet area (A_2) is greater than the flow inlet area (A_1). Therefore, the relative velocity at the outlet (Vr_2) should be slower than the relative velocity at the inlet (Vr_1).

7.1 Centrifugal Fan Inlet

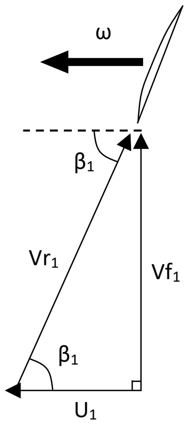

The first step was to find the inlet linear velocity (U_1):

$$U_1 = r_1 \times \omega \Rightarrow U_1 = r_1 \times \frac{N \times 2\pi}{60} \Rightarrow U_1 = 0.035 \times \frac{4000 \times 2\pi}{60} \Rightarrow \underline{U_1 = 14.66ms^{-1}}$$

Afterwards, the flow velocity (Vf_1) was found. For the inlet, the flow velocity is the same as the absolute velocity (V_1) since there was no pre-whirl; therefore, the flow is assumed to enter the blade at no angle, or no tangential component:

$$Vf_1 = \frac{\dot{Q}}{A_1} \Rightarrow Vf_1 = \frac{0.352424}{2 \times \pi \times 0.035 \times 0.05} \Rightarrow \underline{Vf_1 = 32.05ms^{-1}}$$

Since the velocity triangle is a right-angle triangle, the relative velocity (Vr_1) can be found using Pythagoras Theorem:

$$Vr_1 = \sqrt{{Vf_1}^2 + {U_1}^2} \Rightarrow Vr_1 = \sqrt{32.05^2 + 14.66^2} \Rightarrow \underline{Vr_1 = 35.25ms^{-1}}$$

Finally, the inlet blade angle (β_1):

$$\beta_1 = \tan^{-1}\left(\frac{Vf_1}{U_1}\right) \Rightarrow \beta_1 = \tan^{-1}\left(\frac{32.05}{14.66}\right) \Rightarrow \underline{\beta_1 = 65.42^{\circ}}$$

7.2 Centrifugal Fan Outlet

There were important points to consider before performing the outlet calculations. Generally, there are three types of centrifugal fans: backwards curved, radial, and forward curved centrifugal fans. The backwards curved centrifugal fan is the most efficient: it reaches the peak power consumption, and then the power demand drops off within their usable airflow range. They are known as the 'non-overloading fans' since the change in their static pressure does not overload the motor. Radial centrifugal fans are well suited for many ranges of applications due to the high static pressure they can provide. The simple blade design allows them to operate at high temperatures and medium blade tip speeds. Forward curved centrifugal fans operate at lower temperatures and slower blade tip speeds. They are well suited for high airflow applications and are great at moving large volumes of air against relatively low pressures [16] [17]. Figures (32), (33), and (34) show the 3 types of centrifugal fans [18].

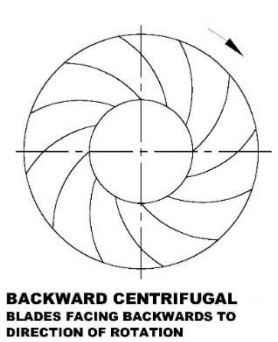

Figure (32): Backward Curved

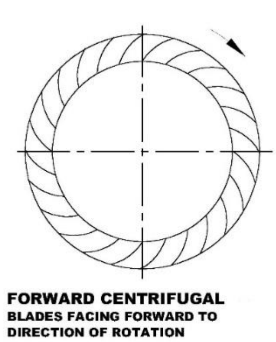

Figure (33): Forward Curved

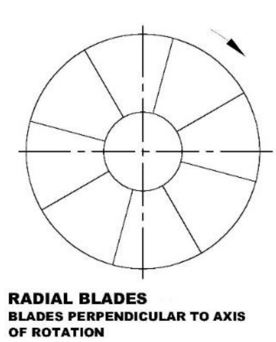

Figure (34): Radial Blades

In this project, the centrifugal fan is quite small, and the volumetric flow rate is quite high. After trial and error, it appeared to be that a forward curved centrifugal fan best suited the application and met the required parameters. The blade outlet angle was set at $\beta_2 = 120^o$, and the rest of the values were calculated as follows.

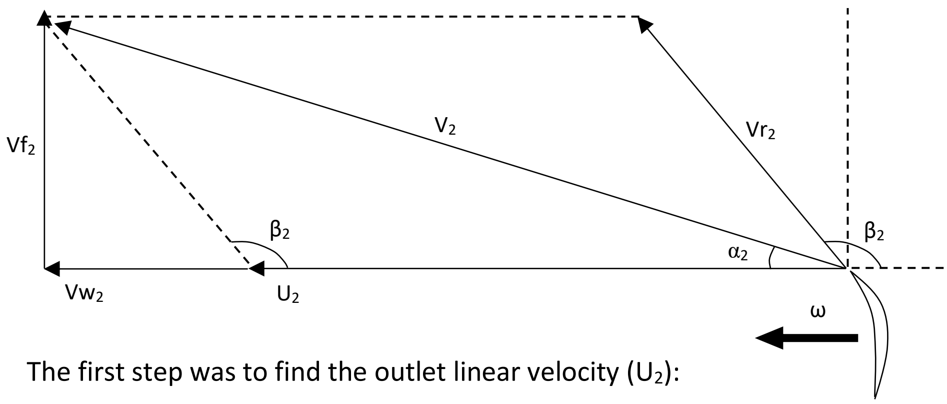

The first step was to find the outlet linear velocity (U_2):

$$U_2 = r_2 \times \omega \Rightarrow U_2 = r_2 \times \frac{N \times 2\pi}{60} \Rightarrow U_2 = 0.05 \times \frac{4000 \times 2\pi}{60} \Rightarrow \underline{U_2 = 20.94ms^{-1}}$$

Afterwards, the flow velocity (Vf_2) was calculated. In the case of the outlet, the flow velocity is not the same as the absolute velocity (V_2) since there is whirl/tangential component (Vw_2), therefore the flow velocity is:

$$Vf_2 = \frac{\dot{Q}}{A_2} \Rightarrow Vf_2 = \frac{0.352424}{2 \times \pi \times 0.05 \times 0.05} \Rightarrow \underline{Vf_2 = 22.44ms^{-1}}$$

The relative velocity (Vr_2) will have the same angle as the blade outlet angle β_2:

$$Vr_2 = \frac{Vf_2}{Cos(\beta_2 - 90)} \Rightarrow Vr_2 = \frac{22.44}{Cos(120-90)} \Rightarrow \underline{Vr_2 = 25.91ms^{-1}} \text{ (Smaller than } Vr_1 \Rightarrow \text{Condition Met)}$$

The absolute velocity (V_2) was found using the Cosine Rule:

$$V_2 = \sqrt{{U_2}^2 + {Vr_2}^2 - 2 \times U_2 \times Vr_2 \times Cos(\beta_2)} \Rightarrow V_2 = \sqrt{20.94^2 + 25.91^2 - 2 \times 20.94 \times 25.91 \times Cos(120)}$$

$\underline{V_2 = 40.65ms^{-1}}$ (Greater than V_1 ➔ Condition Met)

The whirl/tangential velocity component was found using Pythagoras Theorem:

$$Vw_2 = \sqrt{{V_2}^2 - {Vf_2}^2} \Rightarrow Vw_2 = \sqrt{40.65^2 - 22.44^2} \Rightarrow \underline{Vw_2 = 33.89ms^{-1}}$$

Finally, the power and the head were important parameters to specify the motor required and its performance. However, this project's aim is not to design the most efficient centrifugal fan. Rather, the goal is to have a device that delivers the required airflow to the wing:

Power = $\dot{m} \times (U_2 \times Vw_2)$ ➔ $0.431719 \times (20.94 \times 33.89)$ ➔ Power = 306.5 Watts

Head = $g^{-1} \times (U_2 \times Vw_2)$ ➔ $9.81^{-1} \times (20.94 \times 33.89)$ ➔ Head = 72.37m

8. Stators Design

The purpose of the stators is to turn the flow to the correct path. It was calculated in the previous section that the absolute velocity of the air at the centrifugal fan outlet is 40.65ms^{-1}. However, this flow had two components: a radial component of Vf_2 = 22.44ms^{-1}, and a tangential component of Vw_2 = 33.89ms^{-1}. The radial component Vf_2 matched the flow velocity requirements for the wing to provide enough lift. However, the tangential component can be thought of as lost kinetic energy.

The stators made the flow as efficient as possible by converting as much of the tangential velocity to the radial velocity. The initial angle of the stators must match the angle of the outlet absolute velocity. This angle (α_2) was calculated using the velocity components of the outlet absolute velocity:

$$\alpha_2 = \tan^{-1}\left(\frac{Vf_2}{Vw_2}\right) \Rightarrow \alpha_2 = \tan^{-1}\left(\frac{22.44}{33.89}\right) \Rightarrow \underline{\alpha_2 = 33.51^{o}}$$

Afterwards, as the stators move radially outwards, the slope angle of the curve increased up to 90° being radial. The change in angle must be gradual and smooth to avoid any flow detachments and/or recirculation, which could hinder the performance. The stator design is shown in Figures (35) and (36). Both figures show the bottom half body part of the vehicle, upon which the stators are mounted.

Figure (35): Top View of Stators

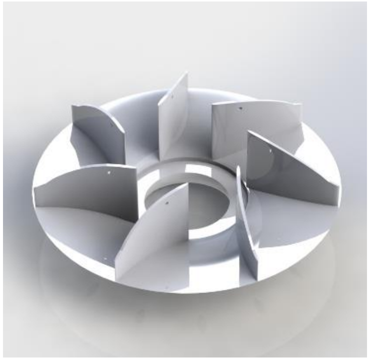

Figure (36): Isometric View of Stators

Finally, the number of veins for the stator must not be equal or be a multiple of the number of blades in the centrifugal fan to avoid any form of resonance that could damage the vehicle. Therefore, the centrifugal fan has 24 blades [17], the stator had 7 veins. Because the stators function was only to direct the flow, having a larger number will reduce the flow area and increase friction; therefore, affecting flow behaviour rather than just fixing flow direction. Moreover, the stators also support the structure connecting the top and bottom halves of the model, so while having less than 7 may be beneficial in terms of flow quality, but the structure may collapse.

9. Experiment

After finilizing the design, an experiment was performed with the setup shown in Figure (37). The goal was to test the wing's performance and the validity of the design. The setup for the experiment was done by placing the model on a wooden stand, with four arms holding the model high to reduce any potential factors interupting the airflow towards the inlet. The whole structure was then placed on a scale to measure the lift force by observing the reduction in mass when the model was operating. Also, an ananometre was used to find the flow velocity at the inlet whilst in operation to obtain mass flow rate. An electric brushless motor was used to drive the centrifugal fan and was powered by an external power source which is the large white box in Figure (37).

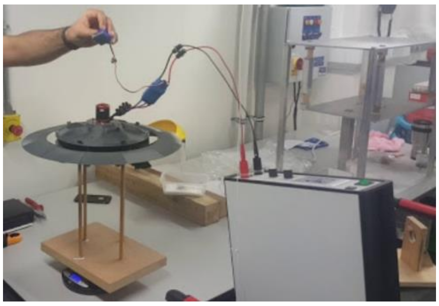

Figure (37): Experiment Setup

The performance of the model was assessed by plotting two graphs to find the relationship between the lift force, and the mass flow rate, against the motor rotational speed. Both are shown below.

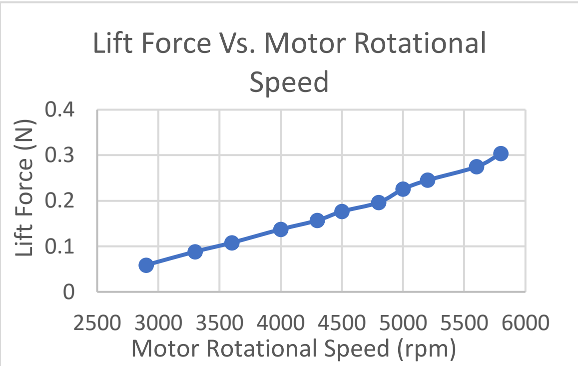

Graph (13): Relationship Between Lift Force and Motor Speed

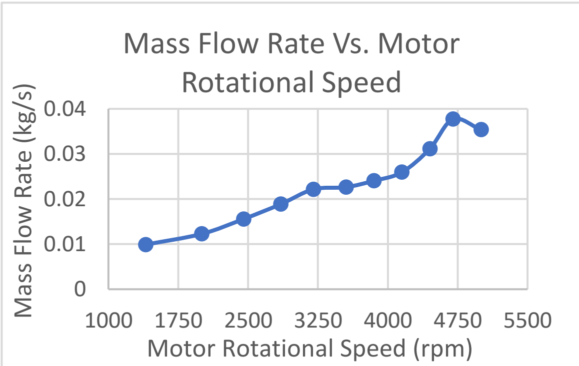

Graph (14): Relationship Between Mass Flow Rate and Motor Speed

As shown in both graphs, as the rotational speed increases, both the lift force and the mass flow rate increase, in almost a linear manner. This proves that the design was stable and consistent. However, at the design condition of 4000 rpm, the lift force produced of approximately 0.14N was far less than what was obtained by the CFD analysis of 3.36N. Also, the mass flow rate of around 0.025kgms^{-1} was far less than the design requirement of 0.432kgms^{-1}. There are few possible reasons for the reduced performance, including: imperfect impeller design, rough duct and wing surfaces, flow detachment on both stator veins and wing, bad airflow quality due to vortices, imperfect wing positioning, manufacturing errors, and the bottom inlet sucking air could be counteracting the lift produced by the wing. Although there was many errors and imperfections, the model was still able to produce lift.

10. Conclusion

This project aimed to understand the aerodynamic behaviour of a circular wing with a duct forcing air against it that could be used in a potential vehicle design as shown in Figure (3). This project proved that this novel design concept is physically possible. Theoretically, the wing should have produced 14.12N of lift; however, the CFD analysis showed it could only produce 3.36N. This reduced value of lift is a result of a combination of factors affecting the wing's performance. Furthermore, the experiment provided physical proof that the vehicle was able to produce lift, but the value was too low: it produced a maximum of 0.31N at 5800rpm which was over the design condition. And at the design condition which was 4000rpm, the lift force produced was only 0.14N.

What was learned from this paper was that the circular wing is a viable option to produce lift. However, at this early stage of the concept's life cycle, the wing is still highly inefficient. Nevertheless, the results were deemed successful, as it proved a concept that has never been tested before. It could have a lot of advantages in terms of stability and control. Compared to conventional crafts, it is predicted to be safer. This paper provided a base point for future research.

While the concept produced positive results, it still has a lot of room for improvement. Possible design enhancements could include a variable AoA, in which the wing can rotate along its circular axis to achieve a variety of angles. Moreover, the addition of primary and secondary control surfaces could increase control and stability and contribute to increased lift force. Better wing positioning to blow air over the wing to achieve maximum pressure difference may significantly increase the lift force. The addition of vortex generators right above the LE of the wing to energise the flow and avoid any potential flow detachment could improve the design. New designs for airfoils may better suit this application. Additionally, a variable height duct to precisely control flow speed, or an advanced stator design to properly direct air flow without any flow detachments may prove to be helpful. The addition of riblets to the inner walls of the duct may reduce the drag factor and increase the overall efficiency. Finally, a new radial impeller or a centrifugal fan's design may better suit the purpose.

During the early stages of aviation, back when the Wright Brothers aircraft concept first flew, the idea was possible, but the technology was still at its early stages. Aircrafts back then were highly inefficient, unsafe, and the opposite of environmentally friendly. But as time passed, thousands of engineers worked, and billions of dollars were spent to create modern aviation tools to produce the safest and the most efficient aircrafts we know today, including the Airbus A380 and the Boeing 787 Dreamliner. The question is: what could this paper's concept amount to if a fraction of the time and effort that was spent on these conventional aircraft was spent on this project? This concept has a lot of unexplored questions yet to be answered. The answers could result in the enhanced future aviation and improved urban transportation.

11. References

[1] Shraideh, S. (n.d.). *Hovering Through New Horizons*. Bachelor of Mechanical Engineering. University of Exeter.

[2] 1. Anthony S. US Air Force’s 1950s supersonic flying saucer declassified [Internet]. ExtremeTech. 2012 [cited 12 June 2018]. Available from: https://www.extremetech.com/extreme/137505-us-air-forces-1950s-supersonic-flying-saucer-declassified

[3] 1. The Avrocar [Internet]. Atlas Obscura. [cited 12 June 2018]. Available from: https://www.atlasobscura.com/places/avrocar

[4] 1. Fedrigo F, Gobato R, Gobato A. Avrocar: a real flying saucer [Internet]. 1st ed. Brazil; 2015 [cited 12 June 2018]. Available from: https://arxiv.org/pdf/1507.06916.pdf

[5] Acrylonitrile Butadiene Styrene (ABS) and Other Specialist Styrenics [Internet]. Bpf.co.uk. 2018 [cited 14 June 2018]. Available from: http://www.bpf.co.uk/plastipedia/polymers/ABS_and_Other_Specialist_Styrenics.aspx

[6] Electric Motors [Internet]. Hobbyking. [cited 20 June 2018]. Available from: https://hobbyking.com/en_us/power-systems/electric-motors.html?___store=en_us

[7] Knoll A. Aerodynamic Analysis. Lecture presented at; 2017; Imperial College London.

[8] Evans P. Properties of Air at atmospheric pressure [Internet]. The Engineering Mind Set. 2015 [cited 25 June 2018]. Available from: http://theengineeringmindset.com/properties-of-air-at-atmospheric-pressure/

[9] Airfoil Tools [Internet]. Airfoiltools.com. [cited August 2018]. Available from: http://airfoiltools.com

[10] ANSYS FLUENT - NACA Airfoil 4412 - CFD.NINJA [Internet]. ANSYS FLUENT – NACA AIRFOIL 4412. 2017 [cited July 2018]. Available from: https://cfd.ninja/ansys-fluent-naca-airfoil-4412/

[11] Choosing the Right Turbulence Model for Your CFD Simulation [Internet]. Engineering.com. 2016 [cited 24 July 2018]. Available from: https://www.engineering.com/DesignSoftware/DesignSoftwareArticles/ArticleID/13743/Choosing-the-Right-Turbulence-Model-for-Your-CFD-Simulation.aspx

[12] Gallardo J. Flat Plate Boundary Layer - Numerical Results - SimCafe - Dashboard [Internet]. Confluence.cornell.edu. 2015 [cited August 2018]. Available from: https://confluence.cornell.edu/display/SIMULATION/Flat+Plate+Boundary+Layer+-+Numerical+Results

[13] Glauert, H.: The Elements of Aerofoil and Airscrew Theory, Cambridge University Press, London, 1926.

[14] Anderson J. Fundamentals of Aerodynamics. Page: 444. 5th ed. John D. Anderson, Jr.

[15] Anderson J. Fundamentals of Aerodynamics. Page: 445. 5th ed. John D. Anderson, Jr.

[16] FANS AND BLOWERS [Internet]. Bureau of Energy Efficiency; [cited 14 August 2018]. Available from: https://www.saylor.org/site/wp-content/uploads/2011/09/Chapter-3.5-Fans-Blowers.pdf

[17] Catalano S, Kaplan K, Plegue T. Visual Encyclopedia of Chemical Engineering [Internet]. Encyclopedia.che.engin.umich.edu. 2018 [cited 20 August 2018]. Available from: http://encyclopedia.che.engin.umich.edu/Pages/TransportStorage/Fans/Fans.html

[18] Working Principle and Types of Air Centrifugal Fans and Blowers [Internet]. Allaboutairblowers.com. [cited 30 August 2018]. Available from: http://www.allaboutairblowers.com/centrifugal-fans-blowers.html

12. Appendices

Appendix (A): Preliminary Design Measurements

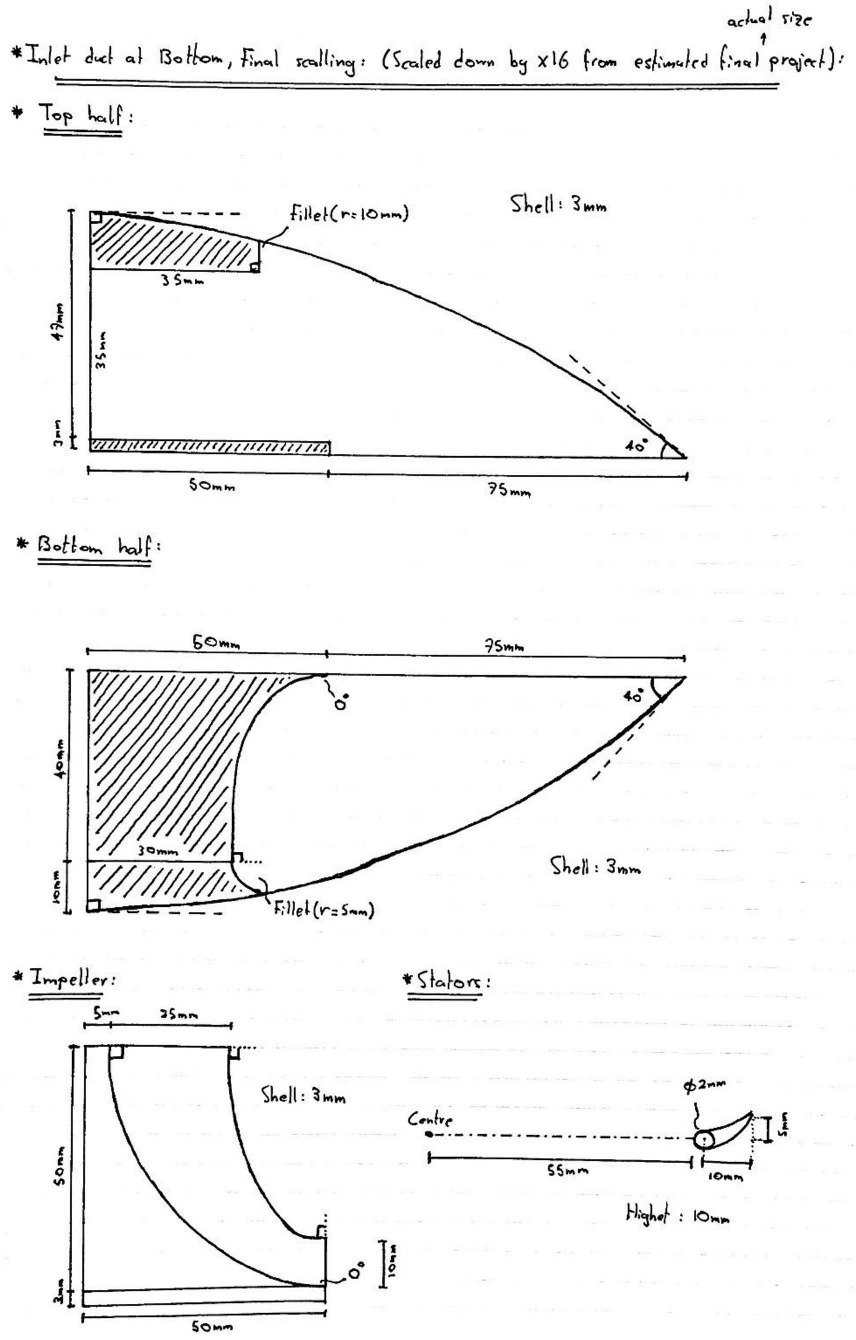

*Wind Shield:

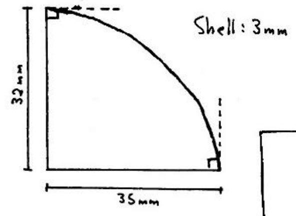

*Wing:

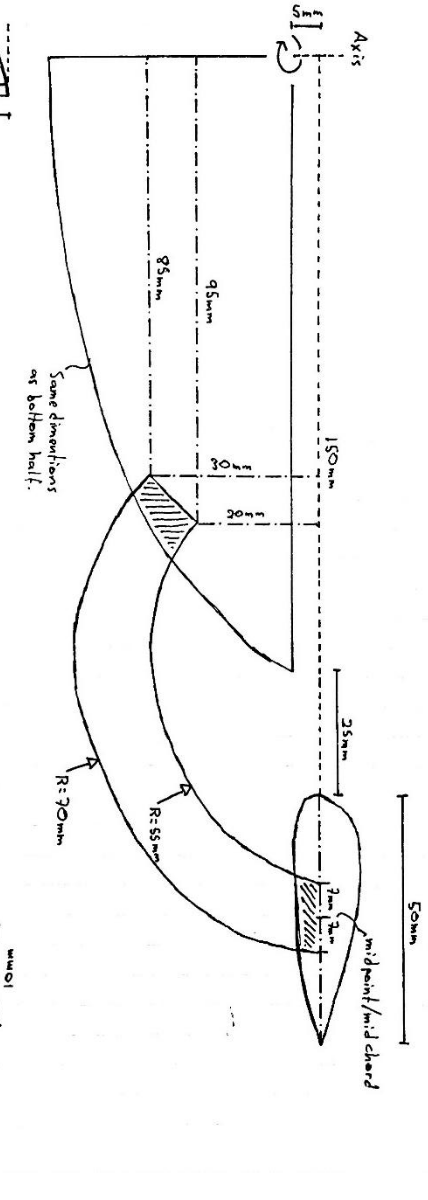

*Control Blades: (X2 size)

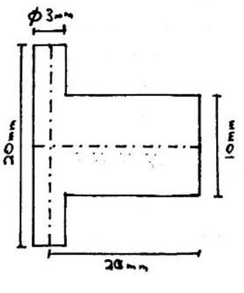

Appendix (B): Final Design Measurements

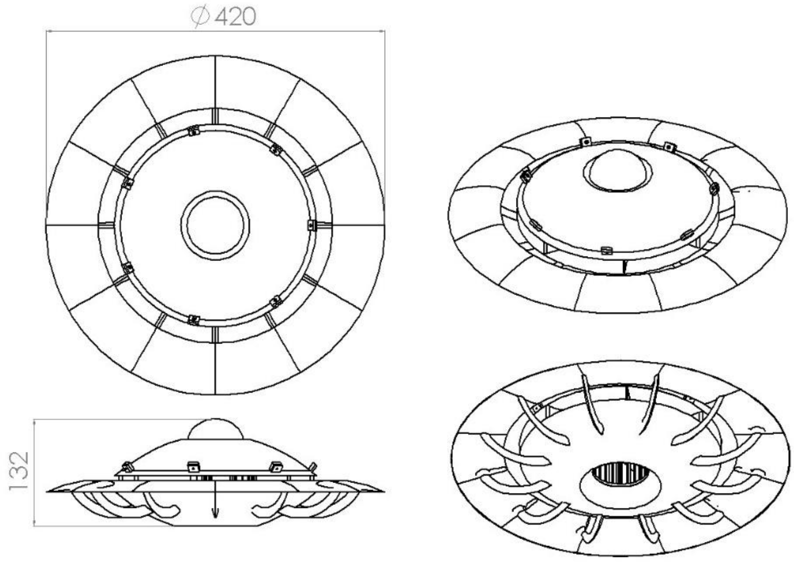

Project Saturn

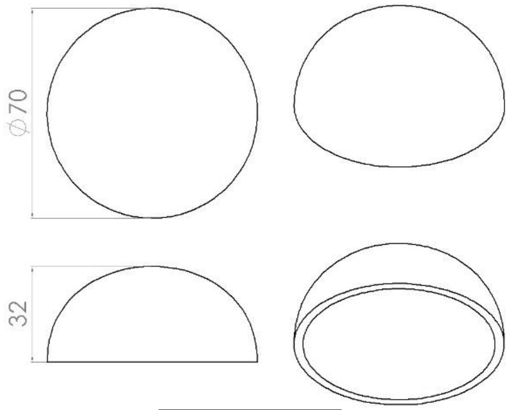

Wind Shield

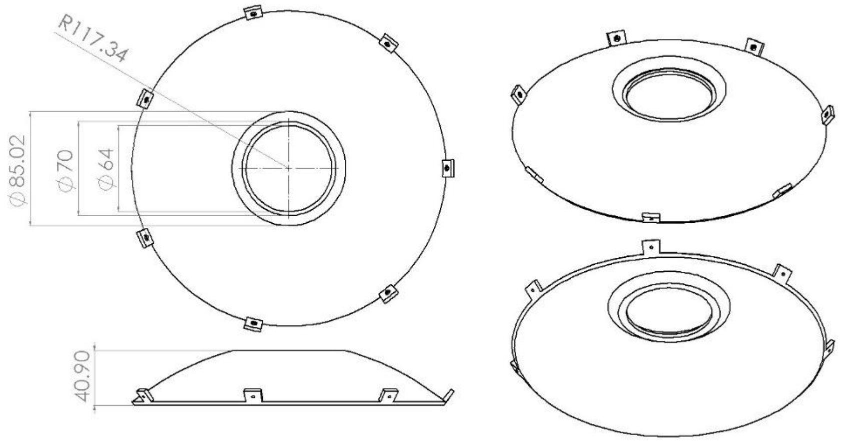

Top Half – Motor Cover

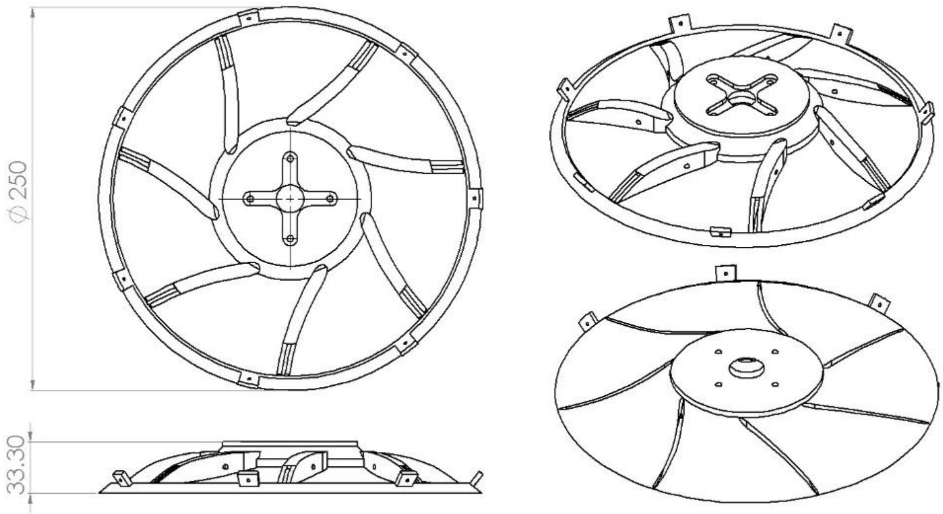

Top Half – Motor Mount

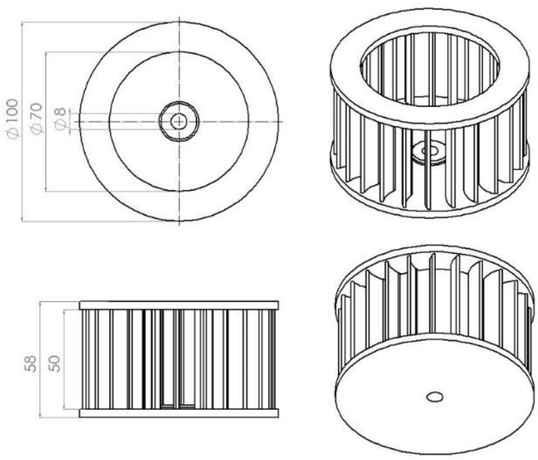

Centrifugal Impeller

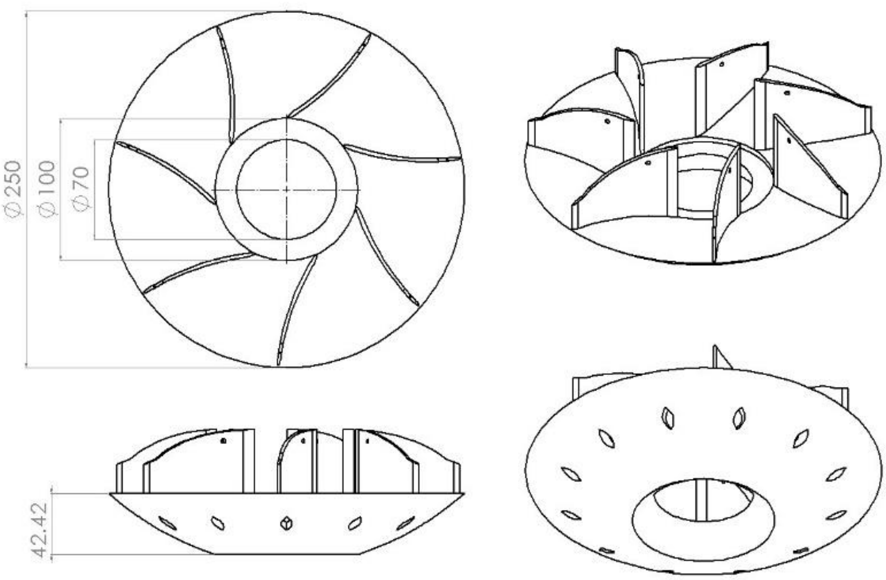

Bottom Half

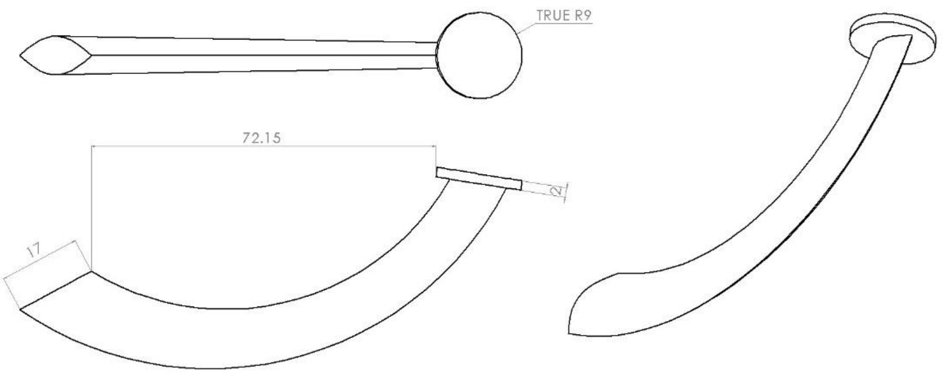

Wing-Body Connector

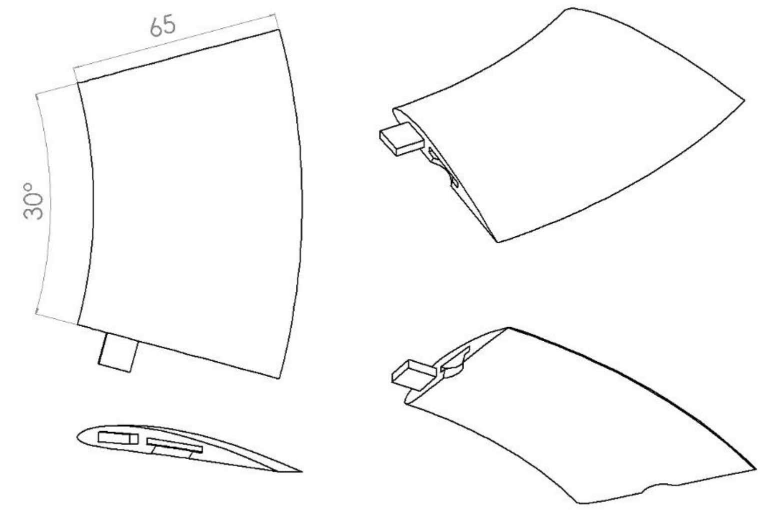

Wing Section

Appendix (C): 25 Test Airfoils and their Geometry

NACA Series Airfoils:

- NACA 4412 (naca4412-il):

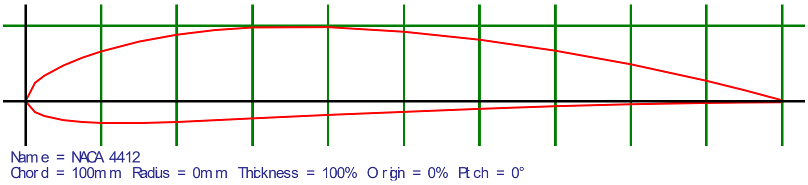

Helicopter Rotor Airfoil:

- AH 79-100 C AIRFOIL (ah79100c-il):

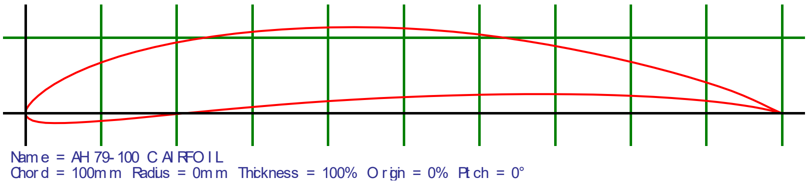

- HUGHES HELICOPTERS HH-02 AIRFOIL (hh02-il):

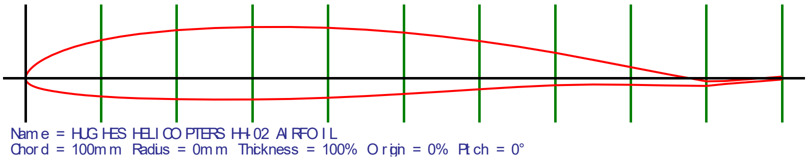

High Lift Airfoils:

- DOUGLAS LA203A AIRFOIL (la203a-il):

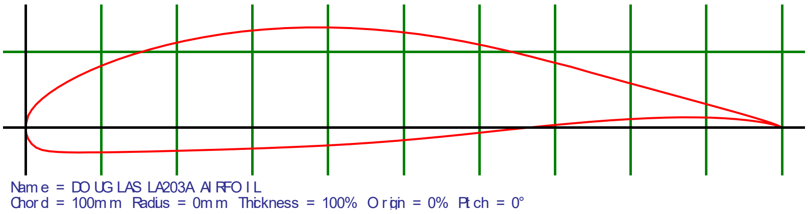

- E423 (e423-il):

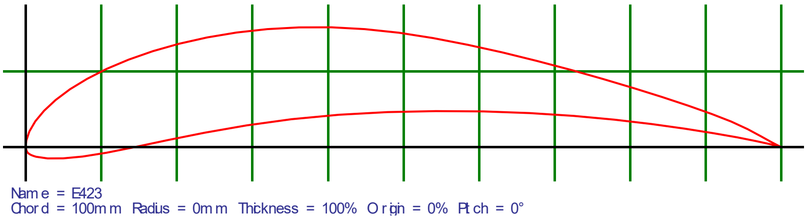

- FX 74-Cl5-140 MOD (smoothed) (fx74modsm-il):

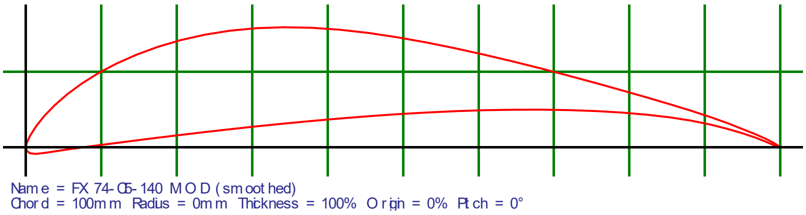

Low Reynolds Airfoils:

- DAE-11 AIRFOIL (dae11-il):

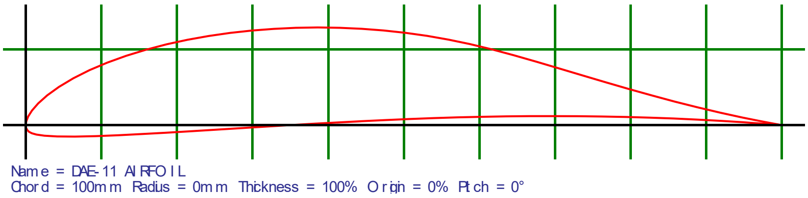

- DAE-31 AIRFOIL (dae31-il):

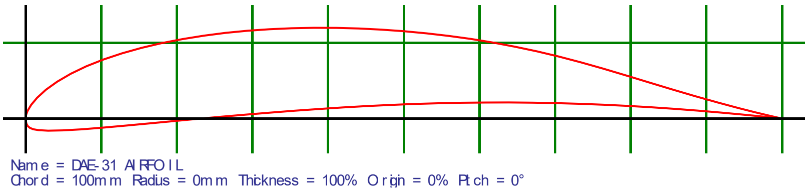

- E205 (10.48%) (e205-il):

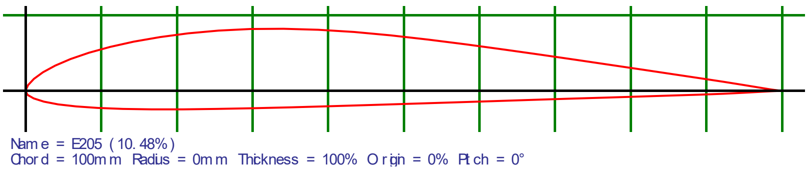

- EPPLER 66 AIRFOIL (e66-il):

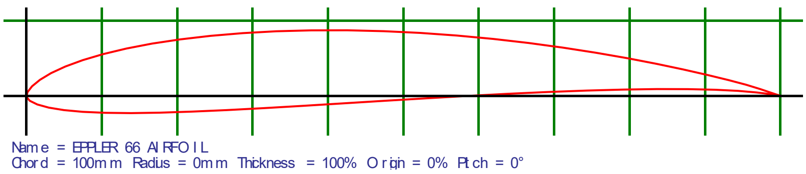

- RG-15 8.9% (rg15-il):

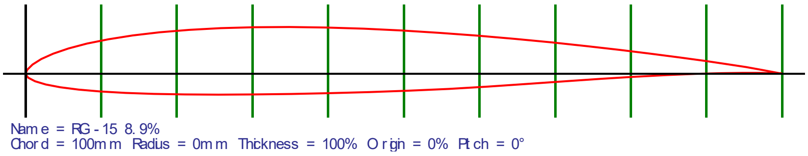

- S2027 (s2027-il):

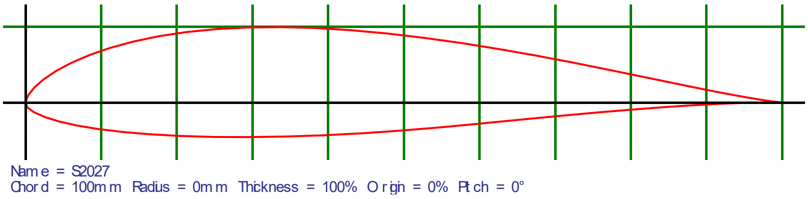

- S7055 (10.5%) Flat-Bottomed (s7055-il):

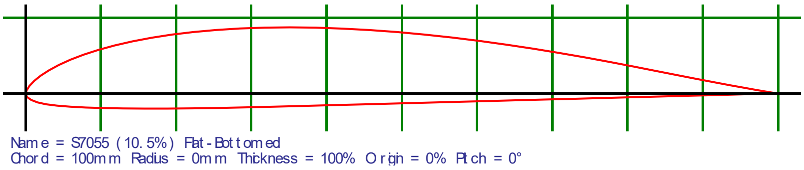

- S8036 (16%) (s8036-il):

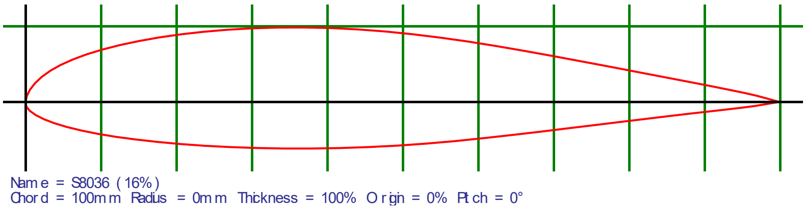

High Lift Low Reynolds Airfoils:

- CH10 (smoothed) (ch10sm-il):

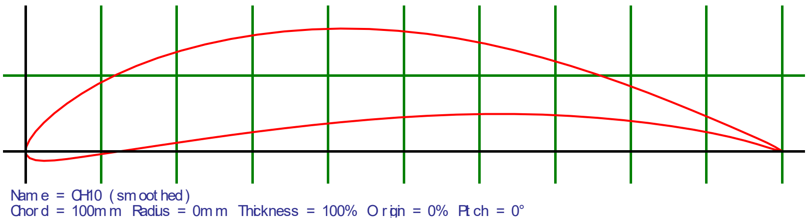

- E387 (e387-il):

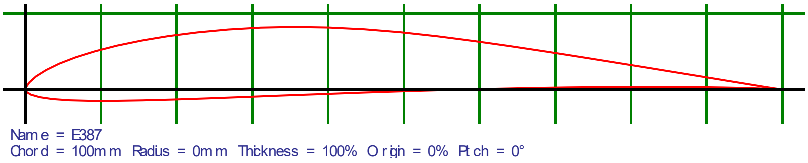

- FX 63-137 (fx63137-il):

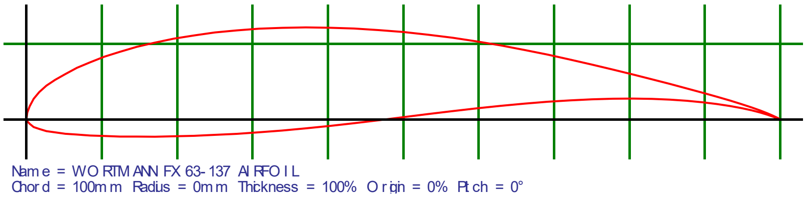

- FX 63-137 13.7% smoothed (fx63137sm-il):

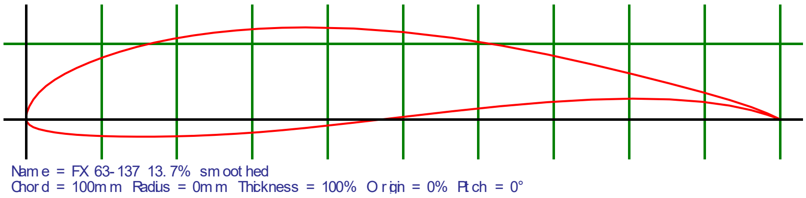

- M06-13-128 (miley-il):

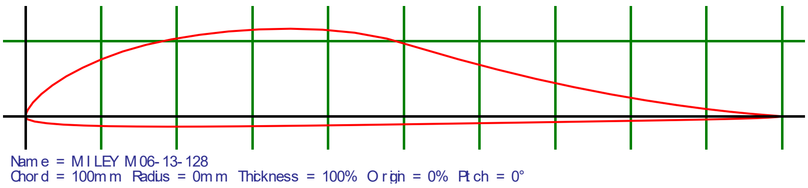

- S1223 (s1223-il):

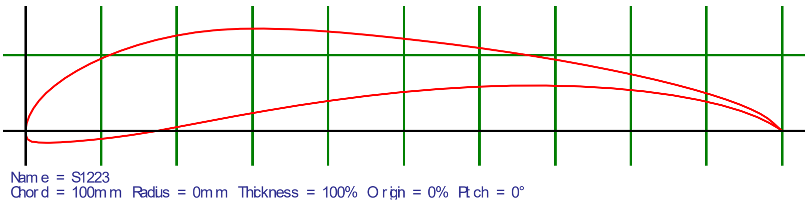

Wind Turbine Airfoils – High L/D Airfoils:

- AH 93-W-145 (ah93w145-il):

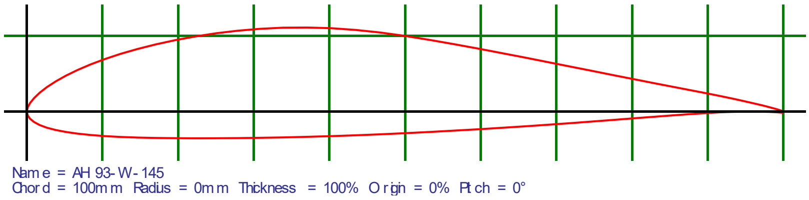

- SG6040 (sg6040-il):

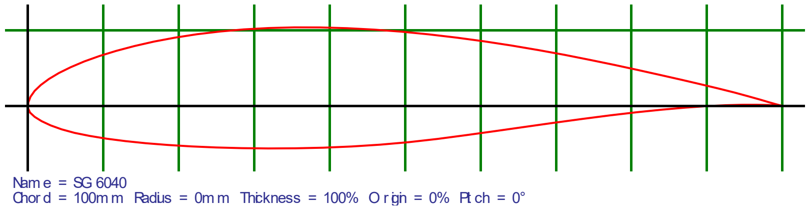

- SG6041 (sg6041-il):

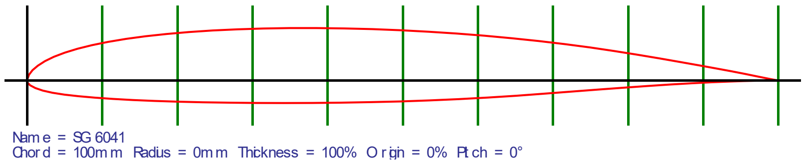

- SG6042 (sg6042-il):

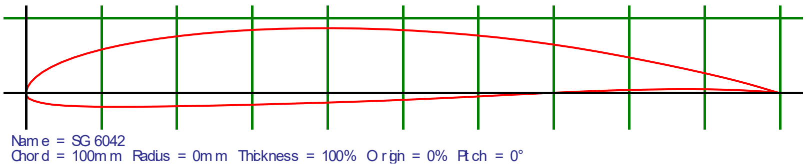

- SG6043 (sg6043-il):

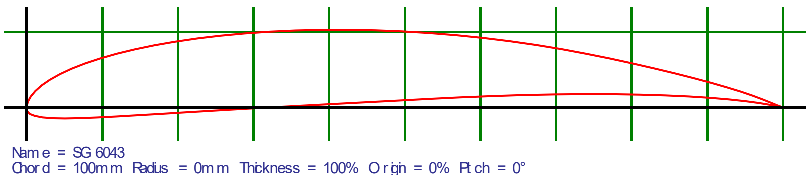

Appendix (D): ‘xflr5’ Analysis Results of the 25 Tested Airfoils

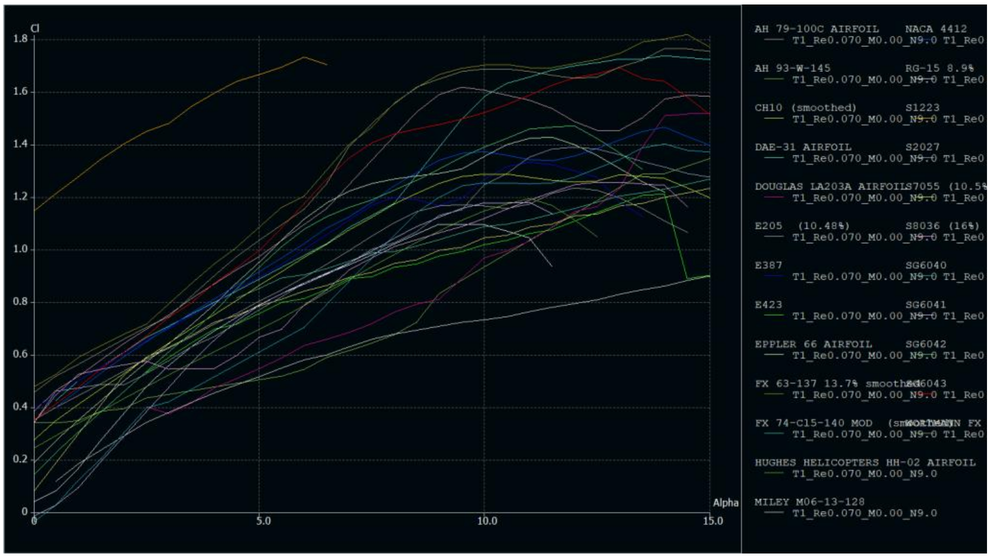

Lift Coefficient Vs. Angle of Attack of the 25 Airfoils at Re=70000

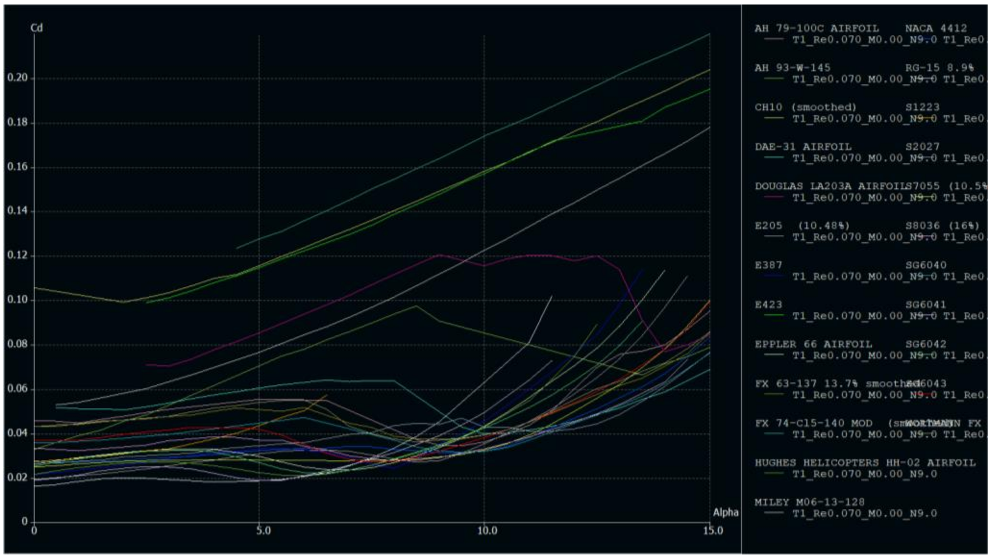

Drag Coefficient Vs. Angle of Attack of the 25 Airfoils at Re=70000

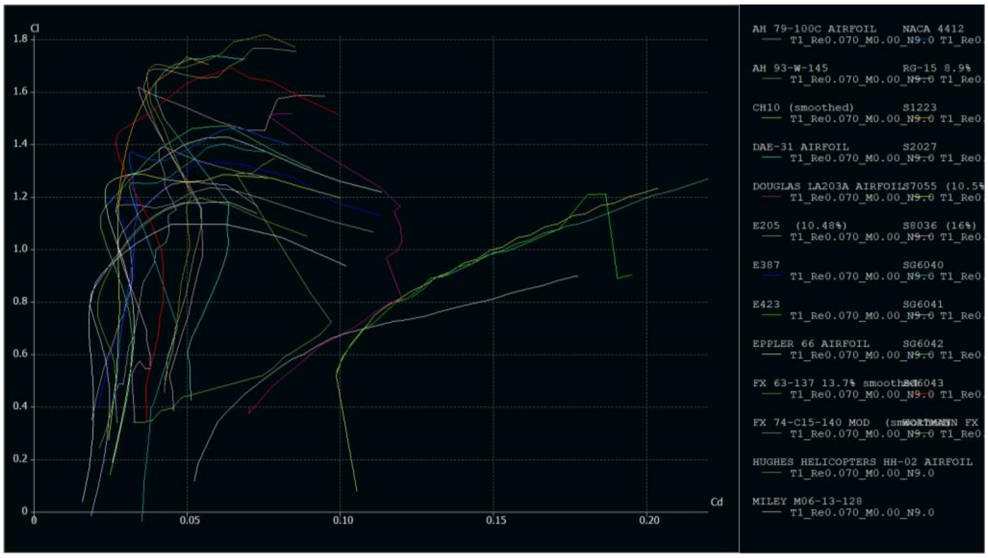

Lift Coefficient Vs. Drag Coefficient of the 25 Airfoils at Re=70000

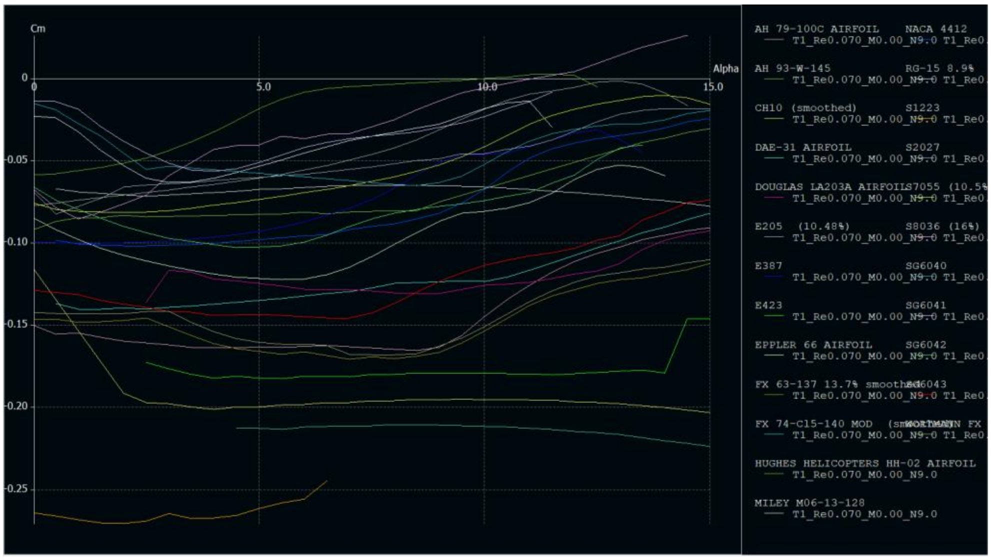

Moment Coefficient Vs. Angle of Attack of the 25 Airfoils at Re=70000

Appendix (E): The Relationship Between Air Velocity and the Change of the Radius of the Exit Duct

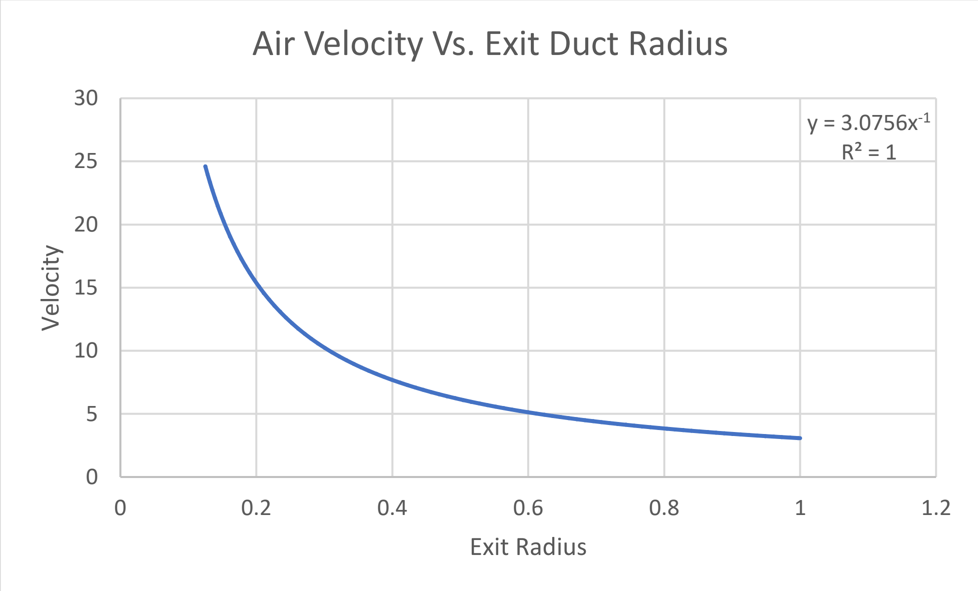

The Change in Velocity as the Exit Duct Radius Increase

Reference Radius	Actual Radius	Reference Velocity	Actual Velocity
0.125	0.125	24.6051	24.6051
0.125	0.126	24.6051	24.40982143
0.125	0.127	24.6051	24.21761811
0.125	0.128	24.6051	24.02841797
0.125	0.129	24.6051	23.84215116
0.125	0.130	24.6051	23.65875000
0.125	0.131	24.6051	23.47814885
0.125	0.132	24.6051	23.30028409
0.125	0.133	24.6051	23.12509398
0.125	0.134	24.6051	22.95251866
0.125	0.135	24.6051	22.78250000
0.125	0.136	24.6051	22.61498162
0.125	0.137	24.6051	22.44990876
0.125	0.138	24.6051	22.28722826
0.125	0.139	24.6051	22.12688849
0.125	0.140	24.6051	21.96883929
0.125	0.141	24.6051	21.81303191
0.125	0.142	24.6051	21.65941901
0.125	0.143	24.6051	21.50795455
0.125	0.144	24.6051	21.35859375
↓	↓	↓	↓
0.125	0.999	24.6051	3.078716216
0.125	1.000	24.6051	3.075637500

Appendix (F): Wing Positioning Data

Exit Duct Radius (m)	Wing LE Radius (m)	Wing TE Radius (m)	Velocity @ LE (ms-1)	Velocity @ Mid-Chord (ms-1)	Air Density (kgm-3)	Chord Length (m)	Dynamic Viscousity (kgm-1s-1) at 15C	Reynolds Number	Re Rounded	Angle of attack	xflr5 Lift Cofficent	3D Lift Coefficient	Wing Planform Area (m2)	Lift Force (N)
0.125	0.15	0.2	20.504	17.57485714	1.225	0.05	0.000017965	69906.48483	70000	9.5	1.364	1.2276	0.054977871	12.76834184
0.125	0.149	0.2	20.64161074	17.6252149	1.225	0.051	0.000017965	71783.16899	72000	9.5	1.364	1.2276	0.055917208	13.06102589
0.125	0.148	0.2	20.78108108	17.67586207	1.225	0.052	0.000017965	73685.21374	74000	9.5	1.367	1.2303	0.056850261	13.38476607
0.125	0.147	0.2	20.92244898	17.72680115	1.225	0.053	0.000017965	75613.13665	76000	9.5	1.367	1.2303	0.05777703	13.68148001
0.125	0.146	0.2	21.06575342	17.77803468	1.225	0.054	0.000017965	77567.46947	78000	9.5	1.367	1.2303	0.058697517	13.97990907
0.125	0.145	0.2	21.21103448	17.82956522	1.225	0.055	0.000017965	79548.7586	80000	9.5	1.369	1.2321	0.059611721	14.30096071
0.125	0.144	0.2	21.35833333	17.88139535	1.225	0.056	0.000017965	81557.56564	82000	9.5	1.369	1.2321	0.060519641	14.6033066
0.125	0.143	0.2	21.50769231	17.9335277	1.225	0.057	0.000017965	83594.46788	84000	9.5	1.369	1.2321	0.061421278	14.90741545
0.125	0.142	0.2	21.65915493	17.98596491	1.225	0.058	0.000017965	85660.05888	86000	9	1.35	1.215	0.062316632	15.00216117
0.125	0.141	0.2	21.81276596	18.03870968	1.225	0.059	0.000017965	87754.94904	88000	9	1.351	1.2159	0.063205703	15.31690972
0.125	0.14	0.2	21.96857143	18.09176471	1.225	0.06	0.000017965	89879.76621	90000	9	1.351	1.2159	0.06408849	15.62233165
0.125	0.139	0.2	22.12661871	18.14513274	1.225	0.061	0.000017965	92035.15629	92000	9	1.351	1.2159	0.064964994	15.92955548
0.125	0.138	0.2	22.28695652	18.19881657	1.225	0.062	0.000017965	94221.7839	94000	9	1.352	1.2168	0.065835216	16.25061689
0.125	0.137	0.2	22.44963504	18.25281899	1.225	0.063	0.000017965	96440.33309	96000	9	1.353	1.2177	0.066699154	16.57397258
0.125	0.136	0.2	22.61470588	18.30714286	1.225	0.064	0.000017965	98691.508	99000	9	1.353	1.2177	0.067556808	16.88716179
0.125	0.135	0.2	22.78222222	18.36179104	1.225	0.065	0.000017965	100976.0336	101000	9	1.353	1.2177	0.06840818	17.20222078
0.125	0.149	0.199	20.64161074	17.67586207	1.225	0.05	0.000017965	70375.65587	70000	9.5	1.364	1.2276	0.054663712	12.84172311
0.125	0.148	0.199	20.78108108	17.72680115	1.225	0.051	0.000017965	72268.1904	72000	9.5	1.364	1.2276	0.055596765	13.13630558
0.125	0.147	0.199	20.92244898	17.77803468	1.225	0.052	0.000017965	74186.4737	74000	9.5	1.367	1.2303	0.056523535	13.46213466
0.125	0.146	0.199	21.06575342	17.82956522	1.225	0.053	0.000017965	76131.03485	76000	9.5	1.367	1.2303	0.057444022	13.76079294
0.125	0.145	0.199	21.21103448	17.88139535	1.225	0.054	0.000017965	78102.41754	78000	9.5	1.367	1.2303	0.058358225	14.06118761
↓	↓	↓	↓	↓	↓	↓	↓	↓	↓	↓	↓	↓	↓	↓
0.125	0.135	0.187	22.78222222	19.10310559	1.225	0.052	0.000017965	80780.82692	81000	9.5	1.369	1.2321	0.052602827	14.48668747
0.125	0.136	0.186	22.61470588	19.10310559	1.225	0.05	0.000017965	77102.74062	77000	9.5	1.367	1.2303	0.050579642	13.90915729
0.125	0.135	0.186	22.78222222	19.16261682	1.225	0.051	0.000017965	79227.34948	79000	9.5	1.368	1.2312	0.051431013	14.24194853
0.125	0.135	0.185	22.78222222	19.2225	1.225	0.05	0.000017965	77673.87204	78000	9.5	1.367	1.2303	0.050265482	13.99608952

Appendix (G): Physical and Numerical Setup for the 2D Inviscid Flow Around the Airfoil

- Physical Setup:
  - Solver Type: Density Based
  - Viscous Models: Inviscid
  - Material: Fluid (Air)
    - Density: 1.225kgm^{-3}
  - Boundary Conditions:
    - Inlet: Velocity Inlet @ 1ms^{-1} x-direction
    - Outlet: Pressure Outlet @ 0Pa
    - Airfoil: Wall – No Slip Condition
    - Operating Conditions:
      - Operating Pressure: 101325Pa
- Numerical Setup:
  - Solution Method:
    - Formulation: Implicit
    - Spatial Discretization:
      - Gradient: Least Squares Cell Based
      - Flow: Second Order Upwind
  - Residual Monitors: Convergence Absolute Criteria for all Residuals at 1×10^{-6}
  - Number of Iterations: Until Convergence, If Not, Until All Variables Stabilized

Appendix (H): Physical and Numerical Setup for the 2D Viscous Flow Around the Airfoil

Spalart-Allmaras:

- Physical Setup:
    - Solver Type: Pressure Based
    - Viscous Models: Spalart-Allmaras – Vorticity Based
        - Options: Curvature Correction
    - Material: Fluid (Air)
        - Density: $1.225 kgm^{-3}$
        - Viscosity: $1.7965\times10^{-5} kgm^{-1}s^{-1}$
    - Boundary Conditions:
        - Inlet: Velocity Inlet @ $15.8ms^{-1}$ @ $\alpha=9.5^{o}$
        - Outlet: Pressure Outlet @ 0Pa
        - Airfoil: Wall – No Slip Condition
        - Operating Conditions:
            - Operating Pressure: 101325Pa
- Numerical Setup:
    - Solution Method:
        - Pressure-Velocity Coupling Scheme: SIMPLE
        - Spatial Discretization:
            - Gradient: Least Squares Cell Based
            - Pressure: Second Order
            - Momentum: Second Order Upwind
            - Modified Turbulent Viscosity: Second Order Upwind
    - Residual Monitors: Convergence Absolute Criteria for all Residuals at 1×10^{-6}
    - Number of Iterations: Until Convergence, If Not, Until All Variables Stabilized

k-epsilon:

- Physical Setup:
  - Solver Type: Pressure Based
  - Viscous Models: k-epsilon – Realizable
    - Near-Wall Treatment: Enhanced Wall Treatment
    - Options: Pressure Gradient Effects and Curvature Correction
  - Material: Fluid (Air)
    - Density: 1.225kgm^{-3}
    - Viscosity: $1.7965\times10^{-5}kgm^{-1}s^{-1}$
  - Boundary Conditions:
    - Inlet: Velocity Inlet @ 15.8ms^{-1} @ α=9.5°
    - Outlet: Pressure Outlet @ 0Pa
    - Airfoil: Wall – No Slip Condition
    - Operating Conditions:
      - Operating Pressure: 101325Pa
- Numerical Setup:
  - Solution Method:
    - Pressure-Velocity Coupling Scheme: SIMPLE
    - Spatial Discretization:
      - Gradient: Least Squares Cell Based
      - Pressure: Second Order
      - Momentum: Second Order Upwind
      - Turbulent Kinetic Energy: Second Order Upwind
      - Turbulent Dissipation Rate: Second Order Upwind
  - Residual Monitors: Convergence Absolute Criteria for all Residuals at 1×10^{-6}
  - Number of Iterations: Until Convergence, If Not, Until All Variables Stabilized

k-omega:

- Physical Setup:
  - Solver Type: Pressure Based
  - Viscous Models: k-omega – SST
    - Options: Low-Re Correction and Production Limiter
  - Material: Fluid (Air)
    - Density: $1.225 kgm^{-3}$
    - Viscosity: $1.7965 \times 10^{-5} kgm^{-1}s^{-1}$
  - Boundary Conditions:
    - Inlet: Velocity Inlet @ $15.8 ms^{-1}$ @ $\alpha = 9.5^{o}$
    - Outlet: Pressure Outlet @ 0Pa
    - Airfoil: Wall – No Slip Condition
    - Operating Conditions:
      - Operating Pressure: 101325Pa
- Numerical Setup:
  - Solution Method:
    - Pressure-Velocity Coupling Scheme: SIMPLE
    - Spatial Discretization:
      - Gradient: Least Squares Cell Based
      - Pressure: Second Order
      - Momentum: Second Order Upwind
      - Turbulent Kinetic Energy: Second Order Upwind
      - Specific Dissipation Rate: Second Order Upwind
  - Residual Monitors: Convergence Absolute Criteria for all Residuals at 1×10^{-6}
  - Number of Iterations: Until Convergence, If Not, Until All Variables Stabilized

Appendix (I): Physical and Numerical Setup for the 3D Straight Wing

- Physical Setup:
  - Solver Type: Pressure Based
  - Viscous Models: k-epsilon – Realizable
    - Near-Wall Treatment: Enhanced Wall Treatment
    - Options: None
  - Material: Fluid (Air)
    - Density: 1.225kgm^{-3}
    - Viscosity: 1.7965×10^{-5}kgm^{-1}s^{-1}
  - Boundary Conditions:
    - Inlet: Velocity Inlet @ 15.8ms^{-1} x-direction
    - Outlet: Pressure Outlet @ 0Pa
    - Wing: Wall – No Slip Condition
    - Symmetry: Symmetry
    - Operating Conditions:
      - Operating Pressure: 101325Pa
- Numerical Setup:
  - Solution Method:
    - Pressure-Velocity Coupling Scheme: SIMPLE
    - Spatial Discretization:
      - Gradient: Least Squares Cell Based
      - Pressure: Second Order
      - Momentum: Second Order Upwind
      - Turbulent Kinetic Energy: Second Order Upwind
      - Turbulent Dissipation Rate: Second Order Upwind
  - Residual Monitors: Convergence Absolute Criteria for all Residuals at 1×10^{-6}
  - Number of Iterations: Until Convergence, If Not, Until All Variables Stabilized

Appendix (J): Physical and Numerical Setup for the 3D Circular Wing

- Physical Setup:
  - Solver Type: Pressure Based
  - Viscous Models: k-epsilon – Realizable
    - Near-Wall Treatment: Enhanced Wall Treatment
    - Options: None
  - Material: Fluid (Air)
    - Density: 1.225kgm^{-3}
    - Viscosity: 1.7965×10^{-5}kgm^{-1}s^{-1}
  - Boundary Conditions:
    - Inlet: Velocity Inlet @ 52.93ms^{-1} Normal to Inlet Boundary
    - Outlet: Pressure Outlet @ 0Pa
    - Wing: Wall – No Slip Condition
    - Top and Bottom Walls: Wall – Allow Slip Condition
    - Symmetry: Symmetry
    - Operating Conditions:
      - Operating Pressure: 101325Pa
- Numerical Setup:
  - Solution Method:
    - Pressure-Velocity Coupling Scheme: SIMPLE
    - Spatial Discretization:
      - Gradient: Least Squares Cell Based
      - Pressure: Second Order
      - Momentum: Second Order Upwind
      - Turbulent Kinetic Energy: Second Order Upwind
      - Turbulent Dissipation Rate: Second Order Upwind
  - Residual Monitors: Convergence Absolute Criteria for all Residuals at 1×10^{-6}
  - Number of Iterations: Until Convergence, If Not, Until All Variables Stabilized

Appendix (K): Physical and Numerical Setup for the 3D Circular Wing

- Physical Setup:
  - Solver Type: Pressure Based
  - Viscous Models: k-epsilon – Realizable
    - Near-Wall Treatment: Enhanced Wall Treatment
    - Options: None
  - Material: Fluid (Air)
    - Density: 1.225kgm^{-3}
    - Viscosity: 1.7965×10^{-5}kgm^{-1}s^{-1}
  - Boundary Conditions:
    - Inlet: Velocity Inlet @ 77.50225ms^{-1} Normal to Inlet Boundary
    - Outlet: Pressure Outlet @ 0Pa
    - Wing: Wall – No Slip Condition
    - Top and Bottom Walls: Wall – Allow Slip Condition
    - Symmetry: Symmetry
    - Operating Conditions:
      - Operating Pressure: 101325Pa
- Numerical Setup:
  - Solution Method:
    - Pressure-Velocity Coupling Scheme: SIMPLE
    - Spatial Discretization:
      - Gradient: Least Squares Cell Based
      - Pressure: Second Order
      - Momentum: Second Order Upwind
      - Turbulent Kinetic Energy: Second Order Upwind
      - Turbulent Dissipation Rate: Second Order Upwind
  - Residual Monitors: Convergence Absolute Criteria for all Residuals at 1×10^{-6}
  - Number of Iterations: Until Convergence, If Not, Until All Variables Stabilized

Appendix (L): Physical and Numerical Setup for the 3D Ducted Straight Wing

- Physical Setup:
  - Solver Type: Pressure Based
  - Viscous Models: k-epsilon – Realizable
    - Near-Wall Treatment: Enhanced Wall Treatment
    - Options: None
  - Material: Fluid (Air)
    - Density: $1.225kgm^{-3}$
    - Viscosity: $1.7965\times10^{-5}kgm^{-1}s^{-1}$
  - Boundary Conditions:
    - Inlet: Velocity Inlet @ $15.8ms^{-1}$ x-direction
    - Outlet: Pressure Outlet @ 0Pa
    - Wing: Wall – No Slip Condition
    - Symmetry: Symmetry
    - Operating Conditions:
      - Operating Pressure: 101325Pa
- Numerical Setup:
  - Solution Method:
    - Pressure-Velocity Coupling Scheme: SIMPLE
    - Spatial Discretization:
      - Gradient: Least Squares Cell Based
      - Pressure: Second Order
      - Momentum: Second Order Upwind
      - Turbulent Kinetic Energy: Second Order Upwind
      - Turbulent Dissipation Rate: Second Order Upwind
  - Residual Monitors: Convergence Absolute Criteria for all Residuals at 1×10^{-6}
  - Number of Iterations: Until Convergence, If Not, Until All Variables Stabilized

Appendix (M): Physical and Numerical Setup for the 3D Ducted Circular Wing

- Physical Setup:
  - Solver Type: Pressure Based
  - Viscous Models: k-epsilon – Realizable
    - Near-Wall Treatment: Enhanced Wall Treatment
    - Options: None
  - Material: Fluid (Air)
    - Density: 1.225kgm^{-3}
    - Viscosity: 1.7965×10^{-5}kgm^{-1}s^{-1}
  - Boundary Conditions:
    - Inlet: Velocity Inlet @ 22.44ms^{-1} Normal to Inlet
    - Outlet: Pressure Outlet @ 0Pa
    - Wing: Wall – No Slip Condition
    - Vehicle: Wall – Allow Slip Condition
    - Top and Bottom Walls: Wall – Allow Slip Condition
    - Wedge Surface: Wall – Allow Slip Condition
    - Symmetry: Symmetry
    - Operating Conditions:
      - Operating Pressure: 101325Pa
- Numerical Setup:
  - Solution Method:
    - Pressure-Velocity Coupling Scheme: SIMPLE
    - Spatial Discretization:
      - Gradient: Least Squares Cell Based
      - Pressure: Second Order
      - Momentum: Second Order Upwind
      - Turbulent Kinetic Energy: Second Order Upwind
      - Turbulent Dissipation Rate: Second Order Upwind
  - Residual Monitors: Convergence Absolute Criteria for all Residuals at 1×10^{-6}
  - Number of Iterations: Until Convergence, If Not, Until All Variables Stabilized